Journal of Structural Geology 169 (2023) 104836

Contents lists available at ScienceDirect

Journal of Structural Geology

journal homepage: www.elsevier.com/locate/jsg

How do inherited dip-slip faults affect the development of new extensional faults? Insights from wet clay analog models

Lorenzo Bonini [a,b,*], Umberto Fracassi [b], Nicolò Bertone [a], Francesco Emanuele Maesano [b], Gianluca Valensise [b], Roberto Basili [b]

[a] Dipartimento di Matematica e Geoscienze, Università di Trieste, Italy
[b] Istituto Nazionale di Geofisica e Vulcanologia, Rome, Italy

ARTICLE INFO

Keywords:
Inherited faults
Extensional basins
Analog modeling
Wet clay models

ABSTRACT

The development of structurally controlled basins is frequently dominated by inherited geological and tectonic structures, especially when the affected region has undergone multiple tectonic phases. In this study we use physically scaled analog models to analyze the impact of inherited faults on the evolution of a new extensional fault system and its associated basin. In our experiments, we introduced inherited faults – bearing diverse geometries and orientations – cut through a homogeneous analog material (wet clay). After each experiment, we compare (a) how the inherited faults affected the inception and development of new faults and (b) the shape of the resulting basins, using a 'reference model' run without pre-existing faults. The results show that the orientation of pre-existing faults with respect to the extensional axis does affect the development of the new extensional structures. The main effects show up when the orientation of the pre-existing faults is closer to that expected for a fault that is optimally oriented (perpendicular) with respect to the direction of extension and has a dip close to an Andersonian extensional fault. Conversely, the impact on the resulting basin shape is more spatially complex, especially in the case of misoriented pre-existing faults. We also compare our experimental results with an analytical method based on the slip tendency theory. The application of our findings to selected natural cases demonstrates how one may interpret the occurrence, orientation, and activity of inherited faults by looking at the present-day geometry and wavelength of an extensional basin, particularly when newly formed extensional faults exhibit structurally unexpected trajectories.

1. Introduction

Extensional basins develop in different geodynamic settings, including continental rifts, back-arc and forearc regions, intra-cratonic areas, or in association with strike-slip tectonics. The normal faults controlling the growth of an extensional basin may be influenced by multiple mechanical characteristics of the structural architecture inherited before the inception of extension (e.g., Childs et al., 2003 and references therein). The spatial distribution of mechanically weak or strong rocks, basement anisotropies, fault reactivations, metamorphic foliation or schistosity, and any pre-existing mechanical discontinuities (weaknesses) are the most critical features controlling the inception and development of extensional faults and their associated basins. Several works addressed this issue, using either analog or numerical models (e.g., Bonini et al., 1997; Michon and Sokoutis, 2005; Aanyu and Koehn, 2011; Autin et al., 2013; Withjack et al., 2017; Zwaan and Schreurs, 2017; Deng et al., 2018; Duclaux et al., 2020; Osagiede et al., 2021; Wang et al., 2021; Zwaan et al., 2021; Corti et al., 2022; Zwaan et al., 2022), or natural cases (e.g., Morley, 1999; Tommasi and Vauchez, 2001; Morley et al., 2004; Bell et al., 2014; Claringbould et al., 2017; Corti et al., 2018; Collanega et al., 2019; Henstra et al., 2019; Pongwapee et al., 2019; Molnar et al., 2020; Wedmore et al., 2020; Bramham et al., 2021).

Likewise, several studies described the reactivation of inherited faults and its effect on the development of new faults in different regions worldwide (e.g., Bonini et al., 1997; Keep and McClay, 1997; Odinsen et al., 2000; Lezzar et al., 2002; Morley et al., 2004; Bellahsen and Daniel, 2005; Corti, 2009; Henza et al., 2010; Frankowicz and McClay, 2010; Nixon et al., 2014; Whipp et al., 2014; Phillips et al., 2016; Deng et al., 2017; Deng et al., 2018; Molnar et al., 2019; Maestrelli et al., 2020), all demonstrating that inherited faults exert a variable control on whether and how new structures unfold.

* Corresponding author. Dipartimento di Matematica e Geoscienze, Università di Trieste, Italy.
E-mail address: lbonini@units.it (L. Bonini).

https://doi.org/10.1016/j.jsg.2023.104836
Received 22 July 2022; Received in revised form 26 February 2023; Accepted 1 March 2023
Available online 5 March 2023

The main elements controlling the reactivation of inherited faults in the brittle upper crust are: a) friction along the fault plane, b) differential strength between faults with respect to the host rocks, and c) orientation of inherited faults relative to the new stress field (e.g., Sibson, 1985). Regarding the latter, some studies investigated how the strike and dip of pre-existing faults in the brittle crust control the development of new faults (e.g., Bellahsen and Daniel, 2005; Henza et al., 2010; Deng et al., 2018; Maestrelli et al., 2020), although their modeling setups essentially focused on the role of strike variability of inherited faults with respect to the new stress field. Nevertheless, a comprehensive study on how the variation of both strike and dip of inherited structures may affect a new extensional system is still lacking. We thus conducted analog experiments simulating different strike/dip classes of inherited faults to fill in this gap, focusing on the role of inherited dip-slip faults. To simulate the effect of those faults, we introduced mechanical discontinuities within a clay pack, their strike and dip spanning the full angle range for each experiment, and compared the results with those obtained in a reference setup, i.e., a model unaffected by inherited faults. To validate our method we then compared our findings with those obtained by a theoretical analysis based on fault reactivation tendency. Finally, we analyzed suitable natural cases to demonstrate how our results may help understanding fault kinematics in regions where ongoing extension overlays a long geodynamic history.

2. Method

Modeling fault reactivation with physical experiments implies a choice among various possible setups and strategies regarding the apparatus design, the analog material, and the technique used to reproduce inherited faults.

Over the years, different extensional apparatuses have been used, depending on the goals of each study (see Zwaan et al., 2019, for a recent discussion on this topic). Among the various options, we selected an experimental box composed of two rigid plates, one is fixed and one is mobile and attached to a stepper motor that generates extension (Fig. 1a), with a brittle layer above it. As demonstrated in previous studies (e.g., Cloos, 1968; Withjack et al., 1990; Eisenstadt and Withjack, 1995; Eisenstadt and Sims, 2005), this configuration imposes a velocity discontinuity (VD) coinciding with the boundary between the mobile and fixed plates, leading to the creation of a graben with a well-developed master fault striking parallel to the VD. We deemed such a configuration appropriate to study how inherited structures impact the development of a single extensional fault.

Among several different analog modeling materials we selected wet clay, that has been used extensively to investigate the evolution of brittle structures in the upper crust, starting from the seminal work by Riedel (1929). Over the years, wet clay has been used to model the evolution of strike-slip (e.g., Tchalenko, 1970; Hempton and Neher, 1986), reverse (e.g., Miller and Mitra, 2011; Bonanno et al., 2017), and normal faults (e.g., Withjack et al., 1990; Spyropoulos et al., 1999; Withjack and Schische, 2006; Henza et al., 2010). One of the reasons for this choice is that the small size of the clay particles and the non-negligible cohesion of the mixture allows for observing the development of fractures and faults with a very high resolution compared to other analog materials (Eisenstadt and Sims, 2005; Reber et al., 2020).

Another feature of our experiment is the introduction of the equivalent of pre-existing faults in the models. Thin mechanical weaknesses in clay models have already allowed the evaluation of the effects of pre-existing faults on the development of new ones (Cooke et al., 2013; Bonini et al., 2014, 2015, 2016; Hatem et al., 2015, 2017; Bonanno et al., 2017; Fedorik et al., 2018). The method for introducing thin mechanical weaknesses exploits the electro-osmotic flow induced by an electric potential difference applied to the wet clay.

We implanted two metal plates connected to the anode of a low-voltage battery at the two opposite corners of our clay cakes (Fig. 1). Then, we connected a blade to the cathode. Introducing the blade in the wet clay package induces water to flow from the wet clay to the blade. Immediately, a very thin film of water envelopes the blade, causing two important effects. The first is to lubricate the blade, easing it to cut through the wet clay without altering the initial shape of the model; the water envelope reduces the dragging effect of the blade, thus preventing it from sticking to the clay walls. The second effect stems from the property of the thin water film attracted by the blade to persist between the two clay walls, thus preventing them from sealing after the blade has cut through.

The velocity of the blade motion is essential to ensure the reproducibility of the ideal friction along the precuts. Notice that the velocity is strictly related to the water content of clay that must be correctly chosen to ensure proper scaling of the models (see Section 2.1 for a detailed description). Also, the applied voltage impacts the blade's ability to attract water molecules; we adopted a 24 V battery. To reduce the variability of the experimental results arising from different running velocities of the blade or uncontrolled dip and strike angles of the simulated inherited faults, we used a robotic arm (collaborative robot model UR5, by Universal Robot; Fig. 1b). The robotic arm was instrumental in reproducing correctly and reliably the chosen geometries (within ± 0.1 mm repeatability error declared by the manufacturer: https://www.universal-robots.com/media/50588/ur5_en.pdf).

2.1. Scaling of analog models

Water content and strain rate are two critical elements to use wet clay as an analog material appropriately (e.g., Eisenstadt and Sims, 2005; Cooke and van der Elst, 2012). We used a mixture of kaolin (*#CC31 China Clay*) with 62% water content by mass, yielding a density of about 1.65 g/cm^3 and cohesion of about 75 Pa (Eisenstadt and Sims, 2005). We adopted a displacement velocity of 1 mm/min, as in previous studies (e.g., Bonini et al., 2014; Bonini et al., 2015; Bonini et al., 2016; Bonanno et al., 2017; Fedorik et al., 2018), to ensure appropriate rheological behavior during the experiments (Cooke and van der Elst, 2012). Our natural target was an upper-crust rock assemblage with a cohesion of 10–20 MPa and a density of 2.5 g/cm^3. Following well-established scaling rules (Hubbert, 1937; Ramberg, 1981), the geometric relationship between the analog model and the natural target can be calculated as follows:

$$l_m = l_n \frac{\rho_n}{\rho_m} \frac{c_m}{c_n}$$

where c is cohesion, ρ is density, and l is length. The subscripts m and n indicate the analog model (m) and the natural target (n), respectively. The equation yields that 1 cm in our models corresponds to 0.9–2.0 km in nature. Our wet clay package was 4.5 cm thick (Fig. 1), which scales to simulate the shallower part of the brittle crust (4–9 km). This thickness, together with the cohesion of the clay mixture, allows us to simulate vertically propagating faults (e.g., Bonini et al., 2015).

Friction coefficient, a further critical parameter, falls in the range of 0.55–0.85 for most rocks located in the brittle upper crust (e.g., Handin, 1966; Byerlee, 1978); in our experiments, we set it at ~0.6, an appropriate value to simulate brittle structures (Bonanno et al., 2017).

2.2. Analog modeling strategy

The stepper motor connected to the mobile plate of our experimental box (Fig. 1) is used to apply 4 cm of total displacement and simulate the development of an extensional basin. For the precuts, we adopted five strike angles – 15°, 30°, 45°, 60°, and 75° – measured clockwise from the direction of the extensional axis to the direction of the precuts, and three dip angles – 30°, 45°, and 60° – yielding 15 different setups (Fig. 1; Table 1). These experimental conditions explored a wide range of geometric configurations to capture most natural cases, including pre-existing contractional or extensional faults in a region that

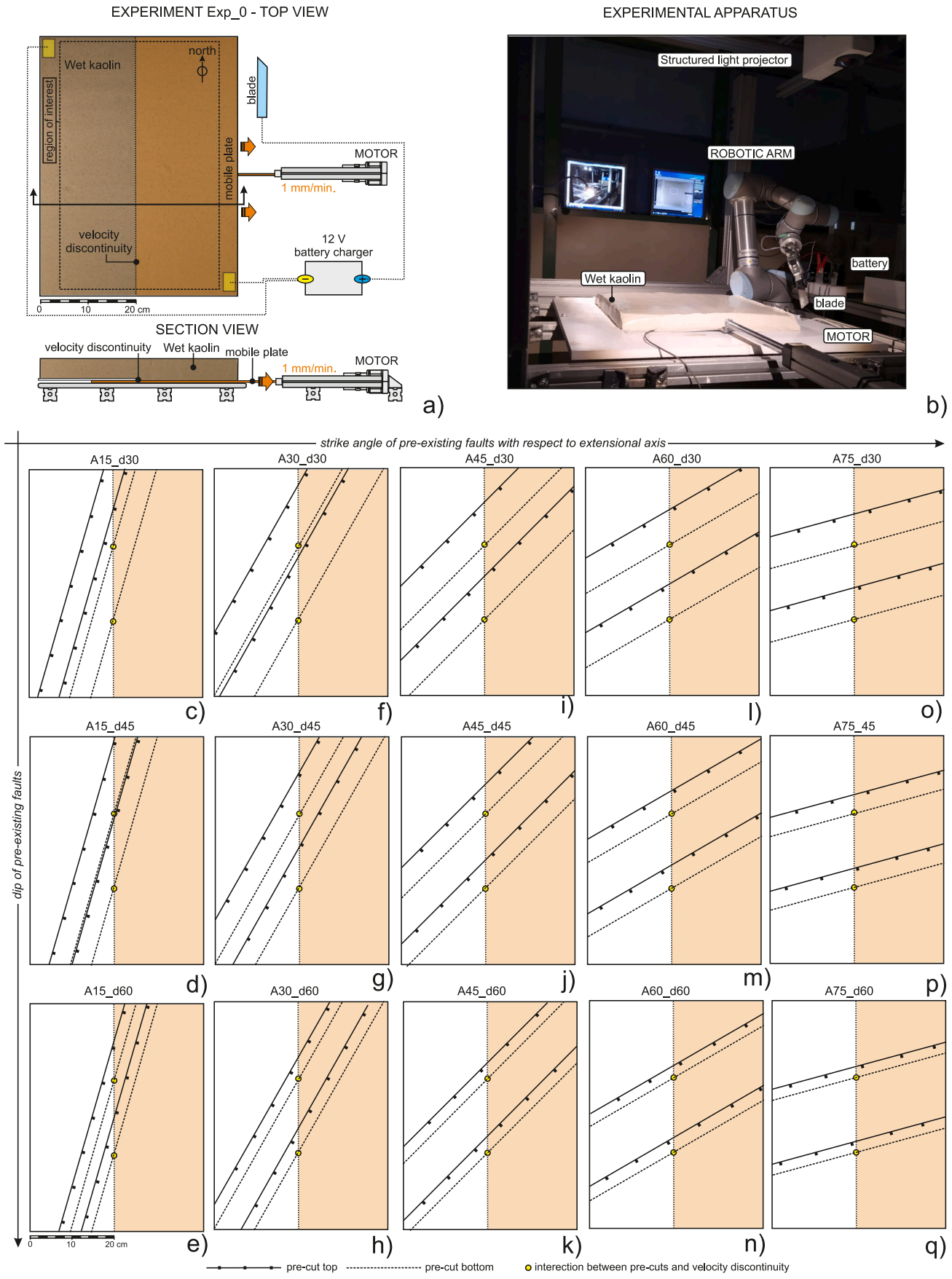

Fig. 1. Sketch (a) and picture (b) of the experimental apparatus and summary (from c to q) of all simulated experimental configurations.

Table 1
Summary of experimental setups. Throughout all experiments, the displacement velocity is 1.0 mm/min, and the maximum base plate displacement is 4 cm (see supplementary material S1).

SETUP	NUMBER OF EXPERIMENTS	STRIKE ANGLE OF PRECUTS (°)	DIP OF PRECUTS (°)
EXP_0	4	NULL	NULL
A15_D30	3	15	30
A15_D45	3	15	45
A15_D60	3	15	60
A30_D30	3	30	30
A30_D45	4	30	45
A30_D60	3	30	60
A45_D30	5	45	30
A45_D45	6	45	45
A45_D60	3	45	60
A60_D30	3	60	30
A60_D45	3	60	45
A60_D60	3	60	60
A75_D30	3	75	30
A75_D45	3	75	45
A75_D60	3	75	60

subsequently underwent an extensional phase. For example, the 30° and 60° dip angles represent Andersonian reverse and normal faults (Anderson, 1951), respectively, while 45° represents both an intermediate angle between the two previous cases and the most common dip for active normal faults (Jackson and White, 1989; Collettini and Sibson, 2001).

A unique code identifies each setup in the form *Axx_dxx*, where *A* and *d* relate to the azimuth and dip angles, respectively. Exp_0 identifies the reference model.

The clay package is 50 × 40 cm in size and laterally unconfined (Fig. 1). We oriented it with the long edges (50 cm) orthogonal to the direction of plate divergence imposed by the stepper motor. The long edge on the fixed plate is referred to as the left edge, and the one on the mobile plate is the right edge. The short edges (40 cm) are those parallel to the direction of extension; they are referred to as the northern and southern edges assuming that all figures have the north in their upper part for a viewer looking at the experiments oriented like in Fig. 1.

Notice that such models may develop undesired (boundary) effects close to the northern and southern edges. As the confining pressure may have a non-negligible effect on the development of structures (e.g., Handin, 1966), we adopted a strategy based on introducing two precuts for each setup instead of just one. The precuts are subject to different confining pressure conditions depending on their distance from the edges. The summary of results (Section 3) represents an average among different behaviors recognized on the two precuts.

Another characteristic of the experimental setups was the common location of the precuts for all configurations with respect to the area undergoing extension. We used two points at the base of the experimental box coinciding with the velocity discontinuity between mobile and fixed plates and equidistant from the northern and southern edges.

To ensure the stability of the experimental results, we repeated each experiment using the same setup at least three times (Table 1).

2.3. Data analysis of analog models

To monitor and analyze the onset and development of new faults, the reactivation along the precuts, and the evolution of basin shapes (subsidence) across all experiments, we took photographs and digital scans of the clay package top surface at each 0.1 cm and 0.5 cm step of mobile plate motion, respectively. We first used photographs to visually monitor the development of fractures and faults during the experiment. Then, we used PIVLab, a software based on the Digital Image Correlation (D.I.C.) method (Thielicke, 2014; Thielicke and Stamhuis, 2014), to compute the incremental horizontal displacement field throughout the experiments based on the photographs. Notice that the displacement field allowed us to detect the incipient activity of faults or precuts well before and beyond the visible deformation that surfaced in the photographs.

The digital scans of the model were obtained using a Structured Light 3D scanning technology (Fig. 1) based on *DAVID-laserscanner* software. The derived 3D models were used to analyze both the fault displacement and the shape of the newly-formed extensional basins, following its deformation for an increasing displacement of the mobile plate.

Following the analytical strategy outlined above, we first show the results of our reference model, named Exp_0, then the results of all other models, broken down by increasing strike (15°, 30°, 45°, 60°, 75°) and dip (30°, 45°, 60°) of the precuts, and listed using the ID criterion outlined in Subsection 2.2. We thus show the topography extracted from the scans and the resulting displacement field calculated using D.I.C. (Fig. 2), which we analyzed to interpret all the experiments, particularly the precut reactivation. All imagery relative to the experiments using precuts can be found in the supplementary material (S1). For each setup with precuts, we opted to stop the experiment after 4 cm of total extension since the reference setup (Exp_0) showed that this is the amount needed by the main extensional structures for bounding entirely the newly formed basin. We also show the lateral view of the structures developed in Exp_0, to be used as a template to assess how fault geometry and kinematics unfold within the model (Fig. 2). Notice that, although data were acquired at 0.1 cm steps, for simplicity we opted to show results obtained at 1.0 cm intervals.

To compare the reactivation of the precuts from the different configurations, we used fault length (L) and maximum displacement (d_{max}), the most commonly used parameters to describe natural faults (e.g., Kim and Sanderson, 2005), which we measured throughout the experiments from topography data.

2.4. Slip-tendency analysis

We applied the slip tendency technique (Morris et al., 1996) to test the ability of our analog modeling setup and strategy to capture the behavior of natural faults to be reactivated.

The ability of an existing cohesionless fault to be remobilized can be evaluated using Amonton's law

$$\tau = \mu_s \sigma_n'$$

where τ is the resolved shear stress on the fault plane, μ_s is the coefficient of sliding friction, and σ_n' is the effective normal stress on the sliding plane. Following Morris et al. (1996), slip on a fault may occur if the resolved shear stress equals or exceeds the frictional resistance to sliding *F* so that

$$F \leq \tau = \mu_s \sigma_n'.$$

Solving this equation for μ_s yields

$$\mu_s = \frac{\tau}{\sigma_n'}$$

from which we obtain the ratio between shear and normal stresses as the *slip tendency* (T_s) of an existing fault by setting.with T_s ranging from 0 to 1. As T_s is equivalent to μ_s, one may assume that if the slip tendency overrides the static friction coefficient of the fault, then slip occurs. This equation means that T_s focuses on the role of the forces acting in a system and provides qualitative estimates of the propensity of a fault plane to be reactivated.

For a given stress regime, the shape of the stress ellipsoid $\varphi = (\sigma_2 - \sigma_3)/(\sigma_1 - \sigma_3)$, which also varies between 0 and 1, affects the slip tendency (Angelier, 1979; Morris et al., 1996). In natural cases, one can extract the stress field using inversion schemes from slip measurements or earthquake focal mechanisms (Neves et al., 2009). T_s and φ can then be used to analyze the reactivation tendency of existing faults.

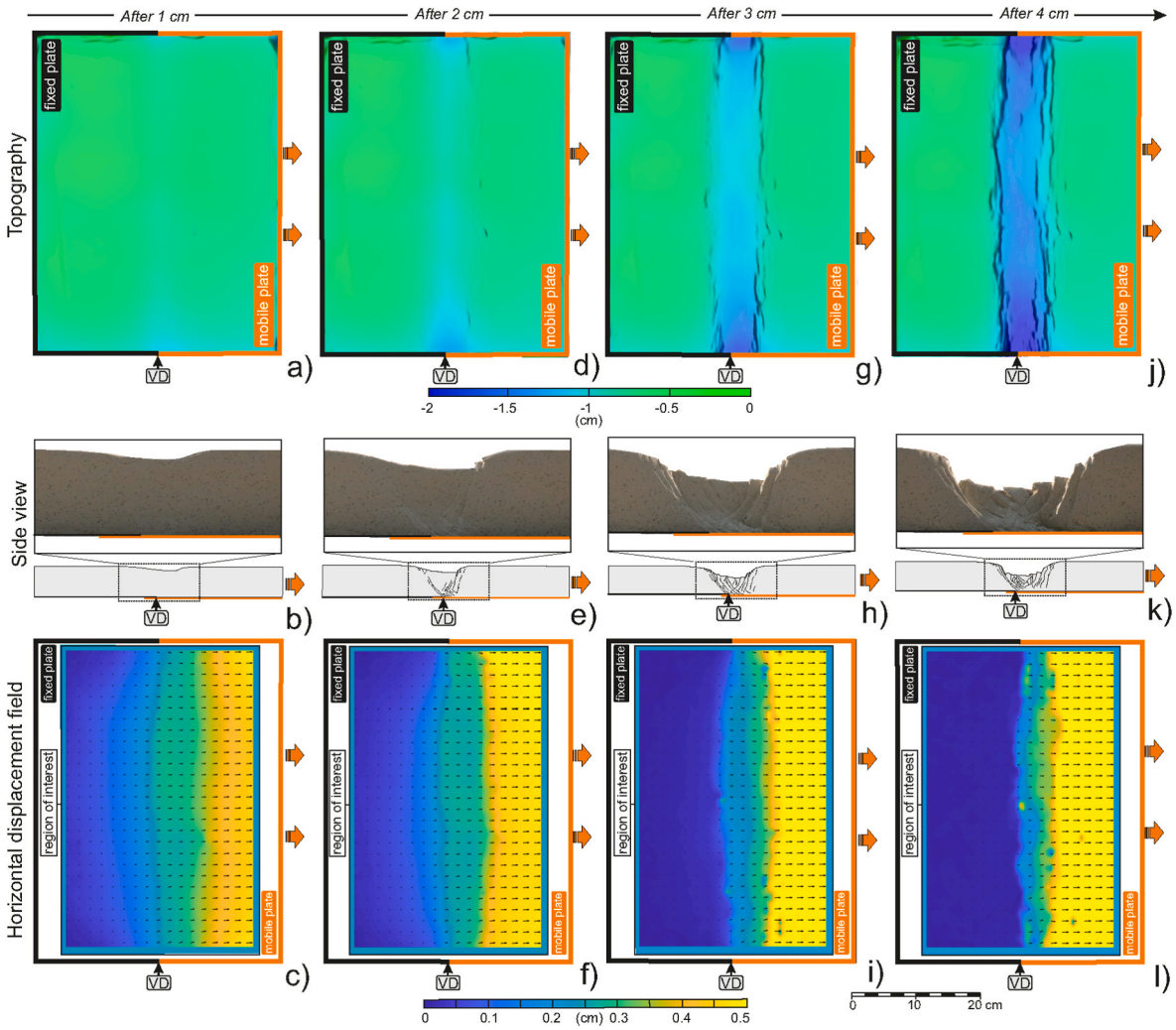

Fig. 2. Map and side views of the *no-precut model* (Exp_0) used as a reference for all subsequent experiments. Each row shows the model development after 1, 2, 3, and 4 cm of base plate displacement. The first row shows the free surface of the models derived by the digital scan with color-coded elevation. The second row shows a line drawing of faults and fractures of the side view of the model and pictures of its central sector after 1, 2, 3, and 4 cm of base plate displacement. The third row shows the incremental displacement field (colors and black arrows) computed using D.I.C. (Digital Image Correlation). In all panels VD shows the location of the velocity discontinuity. (For interpretation of the references to color in this figure legend, the reader is referred to the Web version of this article.)

We exploit this approach to evaluate the theoretical behavior of existing faults similar to those simulated in our experiments. We set up the conditions for the slip tendency analysis, assuming a natural model scaled starting from the dimensions of our analog box (see Subsection 2.1). Thus, we imposed left-right extensional stress to a 9-km-thick volume including planar faults oriented like the precuts across the various analog setups (Fig. 1, Table 1). We then scaled the stress values assuming that, under hydrostatic conditions, the system is tangential to the Mohr-Coulomb envelope at 4.5 km depth for a cohesionless discontinuity and a 30° angle of internal friction (σ_1 vertical at 115 MPa, σ_3 horizontal, left-right oriented at 70 MPa). Finally, we progressively varied φ assigning the same value to σ_2 and σ_1 ($\varphi = 1$) and subsequently reducing it to σ_3 ($\varphi = 0$) in 0.2 steps, so as to account for the impact of stress symmetry on the failure condition (Fjær and Ruistuen, 2002); we hence evaluated the slip tendency T_s at each step.

3. Results

3.1. Reference model (i.e., model with no precuts) – Exp_0

After 1.0 cm of base plate displacement, the top surface of the clay package started subsiding in correspondence of a sharp velocity discontinuity (Fig. 2a, b, and 2c). The amount of subsidence was larger toward the left and right sides of the box, that is, toward the "western" and "eastern" equivalents, respectively, of our experimental setup (Fig. 2a). No faults or fractures were visible on either side of the model, implying that at this stage, displacement was accommodated by folding rather than by faulting and fracturing, which resulted in an asymmetric basin (Fig. 2b).

After 2.0 cm of base plate displacement, a cylindrical basin started developing, becoming clear in the top view (Fig. 2d, e, and 2f); it was more pronounced close to the northern and southern edges, where minor faults and fractures appeared, especially on the right-hand side of the basin (Fig. 2e). Major and minor faults and fractures also developed and became visible; in particular, steep faults dipping to the left affected the right side of the basin, dissecting the free surface of the model (Fig. 2e). Conversely, faults dipping to the right were blind; secondary surface faults cut the free surface (Fig. 2e).

After 3.0 cm of base plate displacement, the shape of the basin was still asymmetric, its subsiding parts still being close to the northern and southern edges of the model (Fig. 2g, h, and 2i). Well-developed faults bounded the right side of the basin over its entire length. Faults on the left side bounded the basin only near the northern and southern edges (Fig. 2g). The side view showed a major fault dipping to the right, while

two faults dipping to the left bounded the basin (Fig. 2h). Finally, several minor faults ruptured through the center of the basin (Fig. 2h).

After 4 cm of extension, the top and side views showed a well-shaped cylindrical basin, bounded on its sides by well-developed extensional faults and arguably in its final arrangement (Fig. 2j, k, and 2l).

3.2. *Experiments with 15°-striking precuts – A15_d30/d45/d60*

These are the experiments where the precuts form a 15° angle with the velocity discontinuity (Fig. 1c, d, 1e, and Figs. 3 and 4).

Starting with the experiment with 30°-dipping precuts (A15_d30; Figs. 1c, 2 and 3), after 1.0 cm of base plate displacement we observed the reactivation of both precuts #1, especially above the fixed plate (Figs. 3a and 4a). The central region of the model showed slight subsidence, coincident with the velocity discontinuity (Fig. 3a). After 2.0 cm of extension (Figs. 3b and 4b), smaller segments of the precuts appeared reactivated, generating an irregularly shaped basin. This effect was enhanced at the end of the next step (after 3.0 cm of extension; Figs. 3c and 4c), when precut #2 became active at the center of the model. After 4.0 cm, the final aspect of the model confirmed this trend, resulting in an irregularly shaped basin (Figs. 3d and 4d).

In the experiment with 45°-dipping precuts (A15_d45), after 1.0 cm of base plate displacement we observed reactivation of the central segment of precut #1 and of the left and right segments of precut #2 (Figs. 3e and 4e). This reactivation immediately impacted the basin shape, as clearly shown after 2.0 cm of extension and until the end of the experiment (Figs. 3f and 4f). Most of this effect was associated with the precut reactivation on the left side of the basin, although precut #2 altered the expected symmetric shape on the right side (Figs. 3g and 4g). At the end of the experiment, the resulting shape of the basin was sigmoidal (Figs. 3h and 4h).

The results from the experiment with 60°-dipping precuts (A15_d60) were similar to the previous case in terms of precut reactivation and basin shape, but the resulting basin was narrower and deeper (Fig. 3i–l,

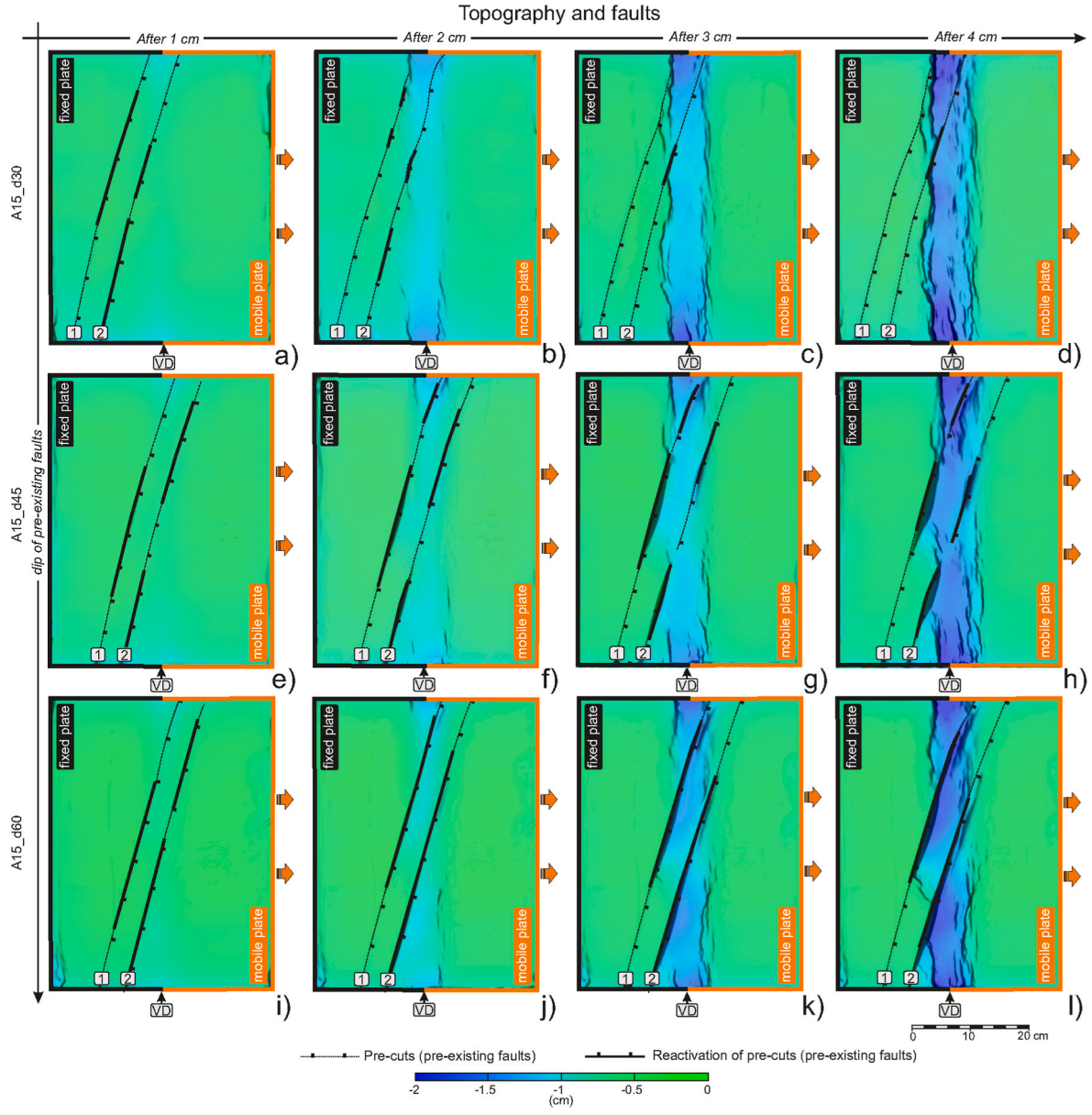

Fig. 3. Free surface of the A15_dxx experiments derived by the digital scan with the color-coded elevation after 1, 2, 3, and 4 cm of base plate displacement. In all panels VD shows the location of the velocity discontinuity. (For interpretation of the references to color in this figure legend, the reader is referred to the Web version of this article.)

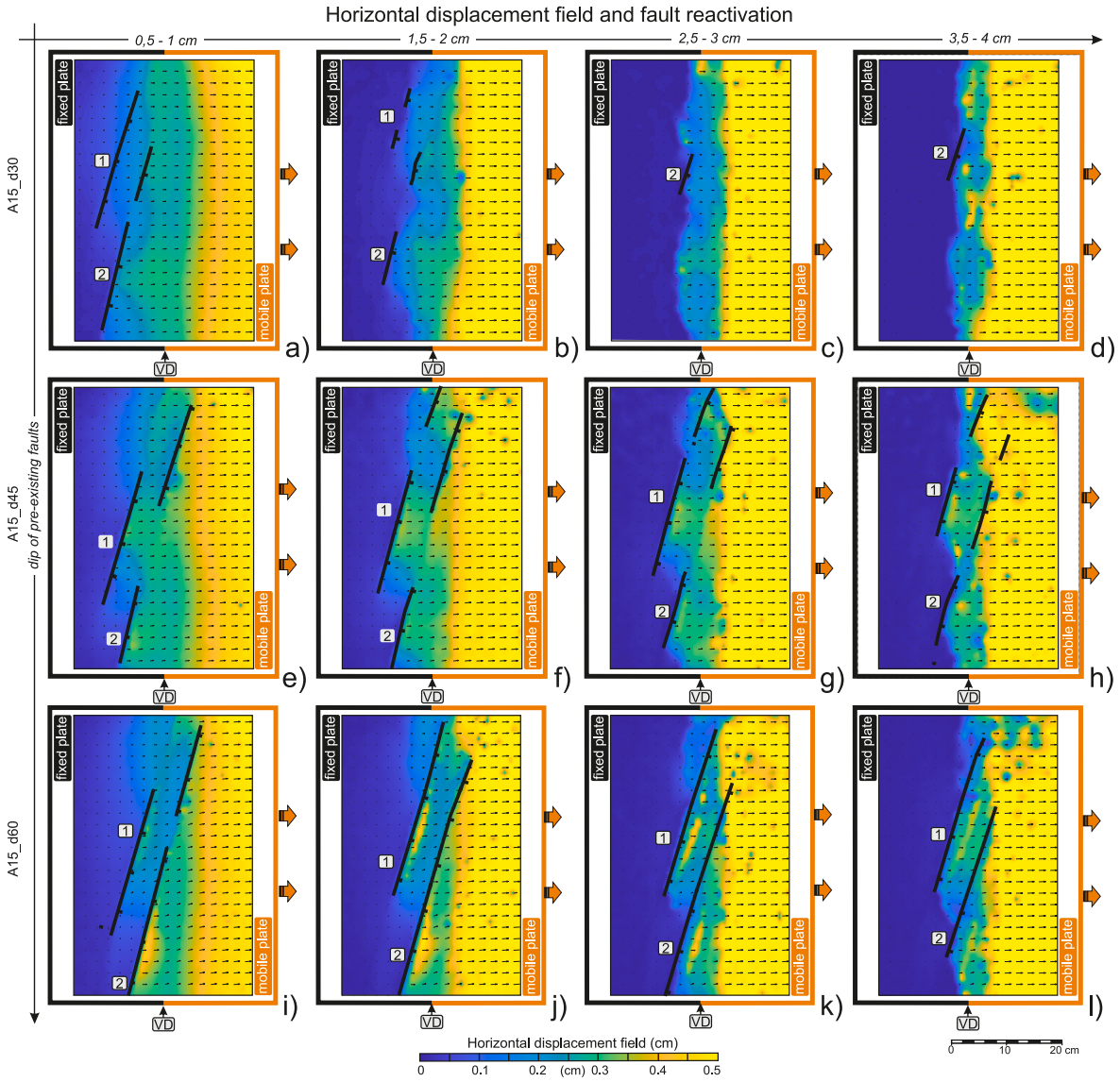

Fig. 4. Incremental displacement field (colors and black arrows) of the A15_dxx experiments computed using D.I.C. (Digital Image Correlation) after 1, 2, 3, and 4 cm of base plate displacement. In all panels VD shows the location of the velocity discontinuity. (For interpretation of the references to color in this figure legend, the reader is referred to the Web version of this article.)

4i- 4l).

3.3. Experiments with 30°-striking precuts – A30_d30/d45/d60

These are the experiments where the precuts form a 30° angle with the velocity discontinuity (Fig. 1f, g, and 1h; Figs. 5 and 6).

After 1.0 cm of base plate displacement, in the experiment with 30°-dipping precuts (Exp_30_30) most precut segments showed reactivation, especially those on the fixed plate (Figs. 5a and 6a). This reactivation decreased during the next step (from 1.0 to 2.0 cm of displacement) on both precuts (Fig. 5b and b). During the following steps and until the end of the experiment (3.0–4.0 cm of displacement), the activity of the precuts was confined within small regions coinciding with the sides of the basin, generating minor anomalies in the basin shape (Fig. 5c, d, 6c, and 6d).

In the experiment with 45°-dipping precuts (A30_d45), after 1.0 cm we observed a widespread reactivation along the precuts, decreasing from the center to the northern and southern edges of the model (Figs. 5e and 6e). The impact of this reactivation on the basin shape became clearer at the end of the second step (i.e., after 2.0 cm; Fig. 5f). The traces of newly formed faults bent and became at a relatively high angle with respect to the precuts (Fig. 5g). By the end of the experiment (i.e., after 4.0 cm), the basin appeared broader than in A30_d30 and Exp_0 (Figs. 2j, 5d and 5h). This basin configuration arose from the coalescence between the subsidence associated with the precut reactivations and that caused by the newly formed extensional faults.

The basin shape anomalies were also visible throughout the experiment with 60°-dipping precuts (A30_d60; Fig. 5i–l). The reactivation of the precuts evolved similarly to that seen in A30_d45 (Figs. 5h and 6h vs. Figs. 5h and 6h); nevertheless, the displacement along the precuts was larger, thus resulting in a narrower and deeper basin, especially close to precut #2 (Fig. 5l).

3.4. Experiments with 45°-striking precuts – A45_d30/d45/d60

These are the experiments where the precuts form a 45° angle with the velocity discontinuity (Fig. 1i, j, and 1k and Figs. 7 and 8).

After 1.0 cm of base plate displacement, in the experiment with 30°-dipping precuts (A45_d30) we observed reactivation of both precuts only in the central part of the model (Figs. 7a and 8a). This reactivation

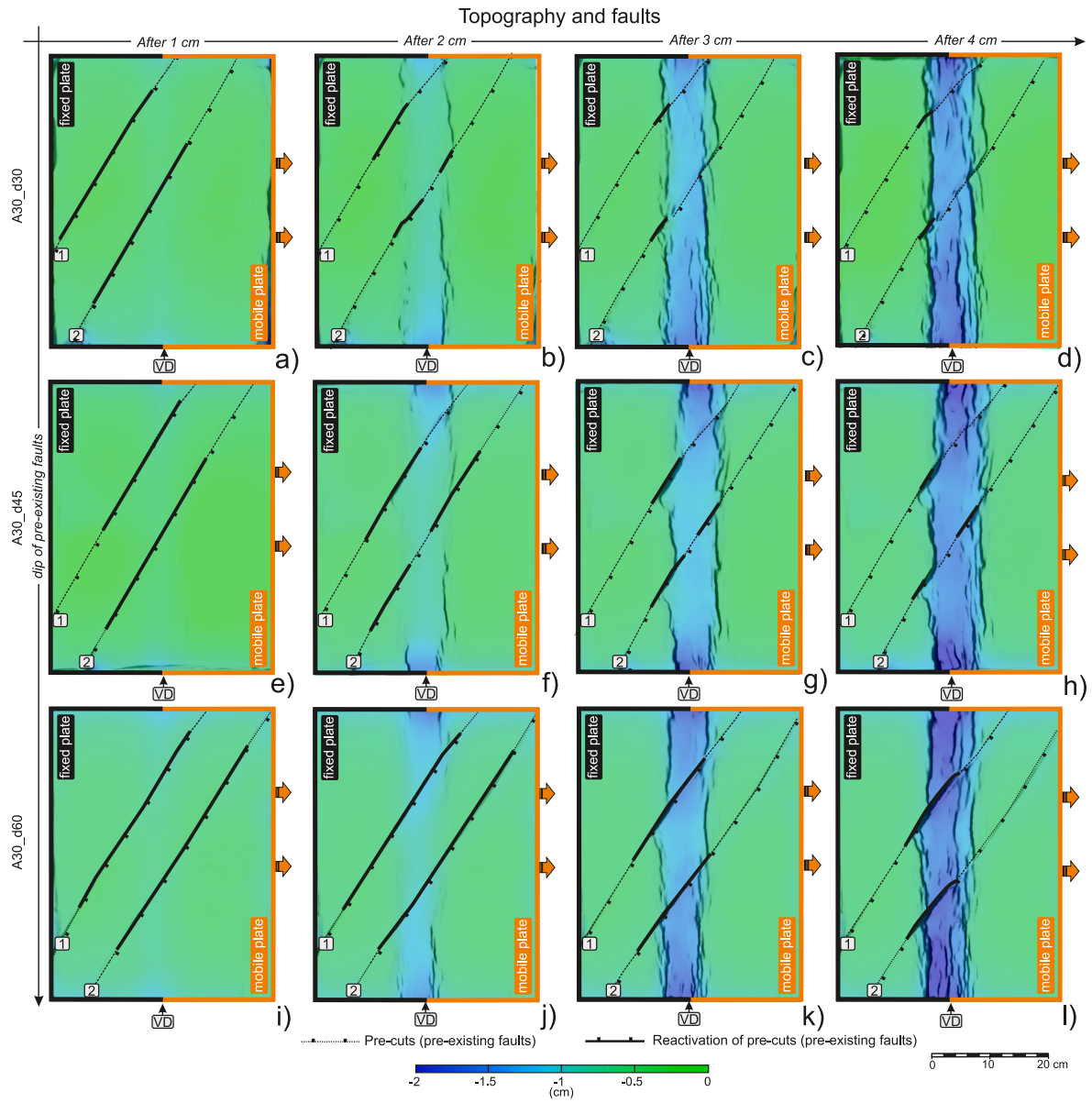

Fig. 5. Free surface of the A30_dxx experiments derived by the digital scan with the color-coded elevation after 1, 2, 3, and 4 cm of base plate displacement. In all panels VD shows the location of the velocity discontinuity. (For interpretation of the references to color in this figure legend, the reader is referred to the Web version of this article.)

decreased during the next step (from 1.0 to 2.0 cm; Figs. 7b and 8b) and disappeared altogether in the remaining steps (2.0–4.0 cm; Figs. 7c–8d). Even if reactivation was limited, the shape of the basin became irregular, showing two broad saddles in the hanging wall of the precuts (Fig. 7d).

In the experiment with 45°-dipping precuts (A45_d45) we observed similar reactivations of the precuts during the first 2.0 cm of displacement (Fig. 7e, f, 8e, and 8f). After 3.0 cm there was no evident reactivation of the precuts (Figs. 7g and 8g). During the last stage (from 3.0 to 4.0 cm), only a small segment of the precuts on the left side of the basin showed reactivation (Figs. 7h and 8h). The resulting basin was wider than that observed in the previous case (A45_d30) and slightly sigmoidal, due to the bending of the newly formed faults as they approached the precuts (Fig. 7h).

The experiment with 60°-dipping precuts (A45_d60) showed a broad reactivation of the precuts in the first interval (up to 1.0 cm of displacement; Figs. 7i and 8i). The reactivation persisted during the next step (1.0–2.0 cm of extension), although to a lesser extent, and focused on the left side of the basin (Figs. 7j and 8j). After 3.0 cm and until the end of the experiment (3.0–4.0 cm of extension) the reactivation of precut segments produced a wider basin than in previous cases; this basin is also more asymmetric due to the bending of the newly formed faults near the precuts (Figs. 7l and 8l).

3.5. Experiments with 60°-striking precuts – A60_d30/d45/d60

These are the experiments where the precuts form a 60° angle with the velocity discontinuity (Fig. 1l, m, and 1n and Figs. 9 and 10).

The experiment with 30°-dipping precuts (A60_d30) showed broad precut reactivations during the first step of deformation (up to 1.0 cm of base plate displacement; Figs. 9a and 10a). No further precut reactivation was detected after 1.0 cm of displacement and up to the end of the experiment. Consequently, the basin and the newly formed faults showed an evolution similar to that shown in the reference model, i.e., the Exp_0 (Figs. 7d and 8d).

The experiment results with 45°-dipping precuts (A60_d45) were similar to those of the previous case, i.e., the A60_d30 (Fig. 9e–h, 10e-

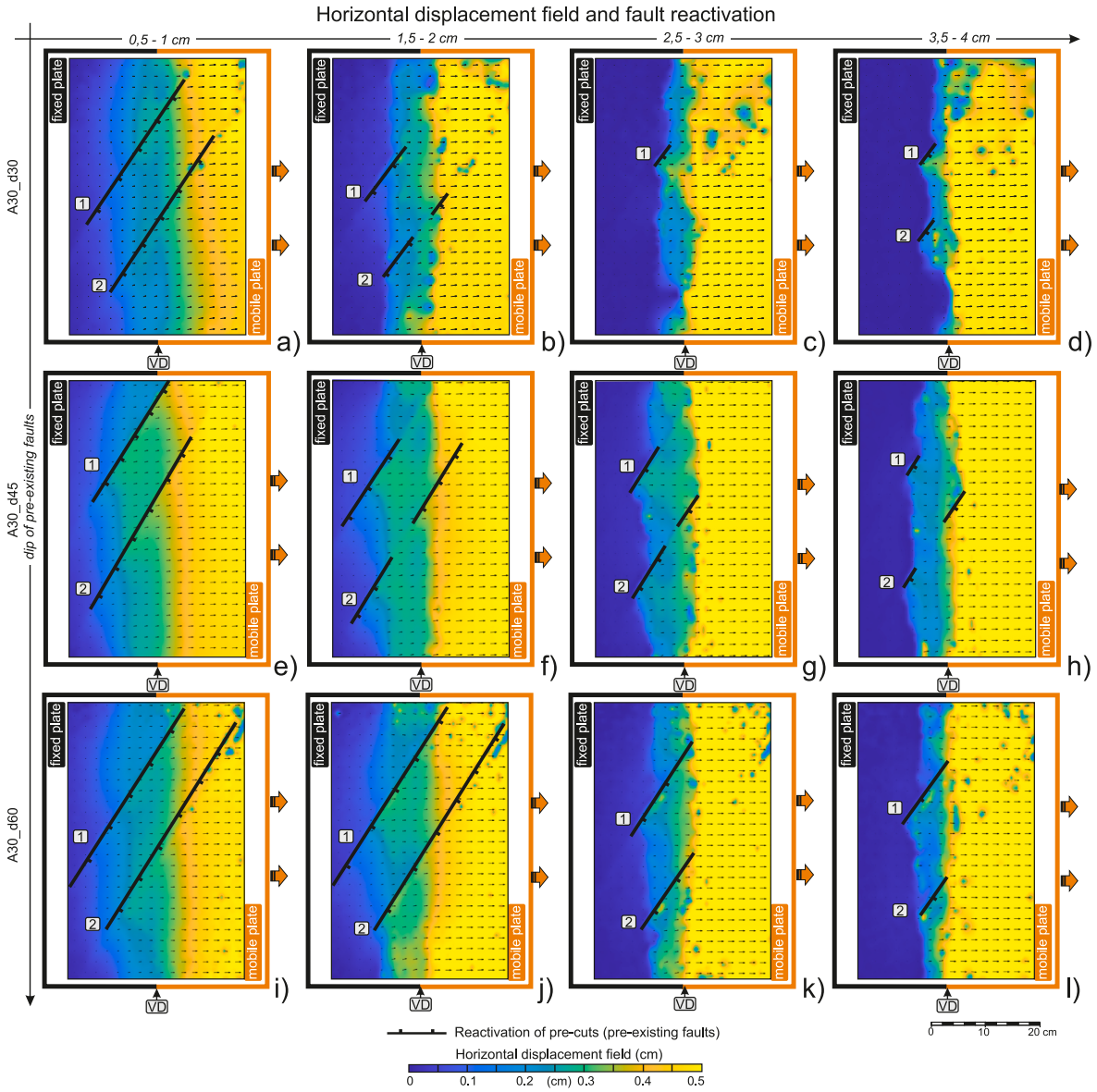

Fig. 6. Incremental displacement field (colors and black arrows) of the A30_dxx experiments computed using D.I.C. (Digital Image Correlation) after 1, 2, 3, and 4 cm of base plate displacement. In all panels VD shows the location of the velocity discontinuity. (For interpretation of the references to color in this figure legend, the reader is referred to the Web version of this article.)

10h).

In the experiment with 60°-dipping precuts (A60_d60) the reactivation was detectable only in the first 1.0 cm of base plate displacement (Figs. 9i and 10i). Even if the precuts did not rupture any further, i.e. no clear reactivation was visible, their limited mobilization seemed to impact the shape of the basin, which widened where newly formed faults interacted with them (Fig. 9l).

3.6. Experiments with 75°-striking precuts – A75_d30/d45/d60

These are the experiments where the precuts form a 75° angle with the velocity discontinuity (Fig. 1o, p, and 1q, and Figs. 11 and 12).

The experiment with 30°-dipping precuts (A75_d30) showed a limited precut reactivation during the first 2.0 cm of base plate displacement (Fig. 11a, b, 12a, and 12b). Nevertheless, it was enough to induce a perturbation of the regular shape of the basin, which appeared narrower at the end of the experiment in the regions where the precuts cross the newly formed faults (Fig. 11d).

The results of the experiments with precuts dipping at 45° and 60° (A75_d45 and A75_d60) are essentially the same as in the previous case (A75_d30), with a tendency for the basin to become narrower where new faults cross the precuts (Fig. 11h and l).

3.7. Summary of the experimental results

As mentioned in Section 2, we introduced two parallel precuts – instead of just one – to reduce the potential over- or under-estimation of the precut reactivations due to the varying confining pressure throughout the experiments. From that, we summarized the experimental results using the average length of the reactivated precuts, the average d_{max} of the new faults in the uncut model, and the average d_{max} of the reactivated precuts (Fig. 13).

The length of the reactivated segments generally decreases from the beginning to the end of the experiments (Fig. 13a). Such behavior is very pronounced in the experiments where reactivation does not affect the final shape of the new basin, and less so in the other ones. For instance, the first group of experiments with a large strike angle, such as A60_dxx and A75_dxx, showed shorter reactivated segments restricted to the

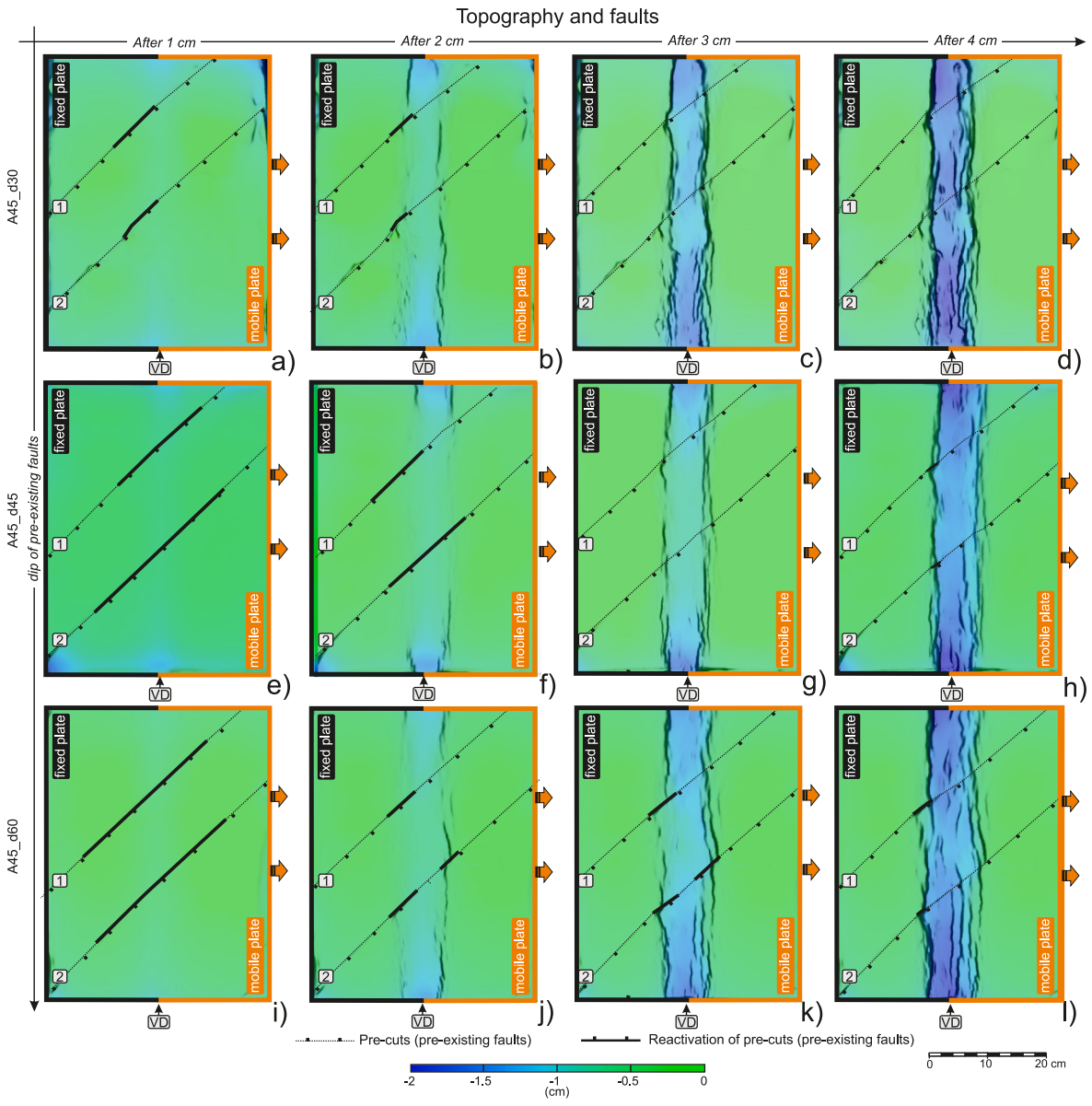

Fig. 7. Free surface of the A45_dxx experiments derived by the digital scan with the color-coded elevation after 1, 2, 3, and 4 cm of base plate displacement. In all panels VD shows the location of the velocity discontinuity. (For interpretation of the references to color in this figure legend, the reader is referred to the Web version of this article.)

early phase of extension (Fig. 13a). In the second group of experiments showing reactivation, the activity of the precuts persisted until the end (Fig. 13a). These observations imply that reactivation may have a different meaning in the two groups. Reactivation in the first group could be related to weak remobilization of the precuts due to an internal stress shift during the first phase of relative motion of the two plates. For the second group, the length of the reactivated segments decreased as the experiment progressed, conceivably due to the increasingly localized extension along the velocity discontinuity area and less connection between the two blocks due to the development of the new faults.

Fig. 13b shows the evolution of d_{max} throughout the experiment along the reactivated segments, compared to the d_{max} of the main fault located in the left portion of the basin for the reference (uncut) experiment. The growth trend of d_{max} in the uncut experiment is variable, showing a steeper gradient when the fault begins to break through the topographic surface (after 2.0 cm of extension), and a flatter gradient during the fourth centimeter of extension. This behavior relates to the different phases of fault development. In the early phase of extension, the new master fault is confined at depth, and most of the stress in the upper level of the clay package is accommodated by folding rather than faulting, namely with a fold-propagation faulting mechanism (Fig. 2). Conversely, in the other experiments, the pre-cuts start to accumulate displacement since the early stages, and the evolution of d_{max} appears quite linear. However, the respective trends show different angular coefficients and final values (Fig. 2b). This suggests that the pre-existing discontinuities act as the master fault of the system during the early stages of deformation because strain concentrates along them. They are secondary and passive features, however, responding to a deeper unfolding process, still not fully developed.

Previous observations of the basin evolution described in Section 3.1 suggest that our results can be subdivided into two groups. The first group shows no reactivation of the precuts after the early phase of extension and no large departures of the basin from a cylindrical shape; this group includes setups where the strike of precuts forms a large angle with the trend of extension (≥60°) and dips at a low angle (30–45°), such as A60_d30, A60_d45, A75_d30, A75_d45, and A75_d60 (Fig. 14).

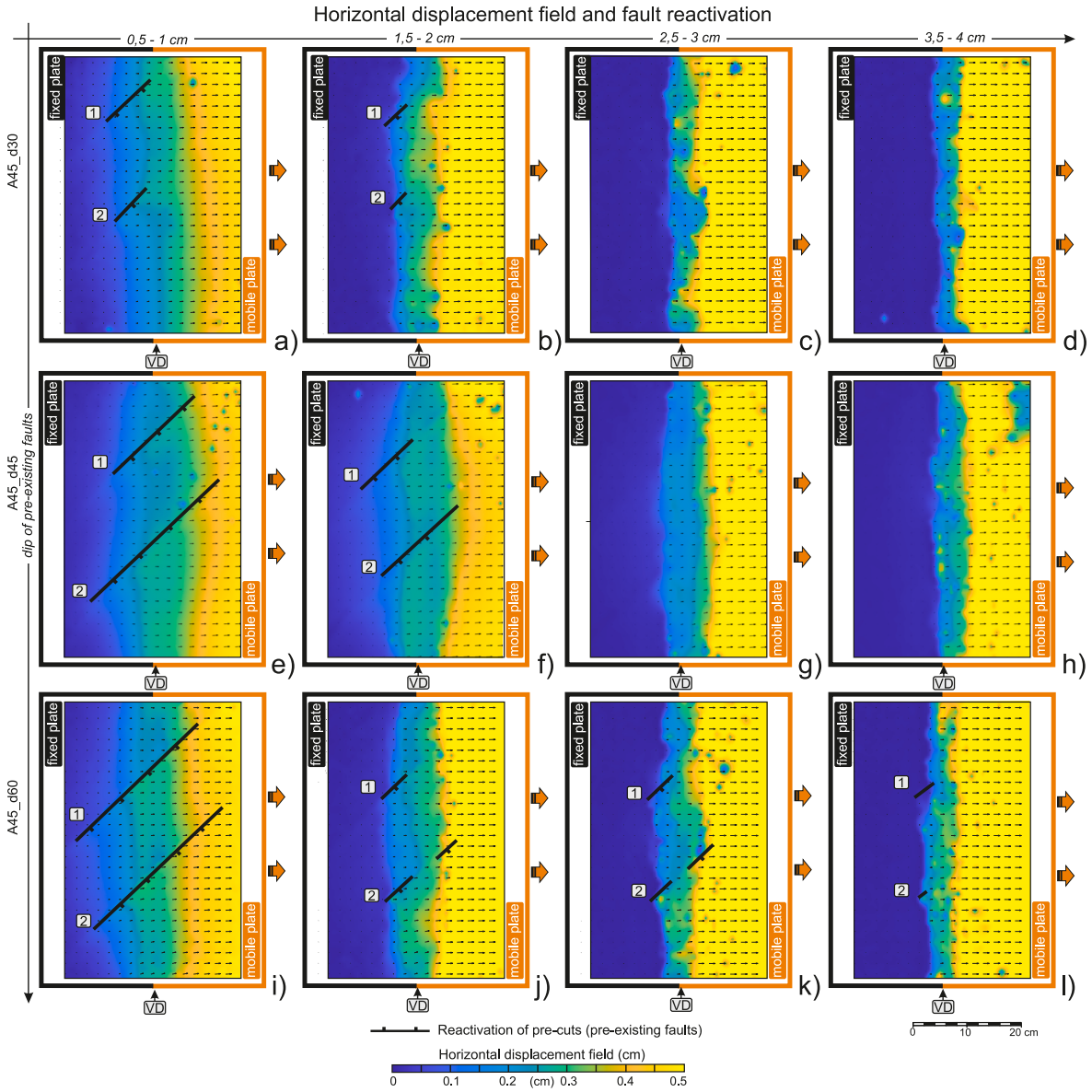

Fig. 8. Incremental displacement field (colors and black arrows) of the A45_dxx experiments computed using D.I.C. (Digital Image Correlation) after 1, 2, 3, and 4 cm of base plate displacement. In all panels VD shows the location of the velocity discontinuity. (For interpretation of the references to color in this figure legend, the reader is referred to the Web version of this article.)

The second group includes all remaining cases. These cases show reactivation of the precuts, which either widened or narrowed various portions of the basin, implying a departure from a purely cylindrical shape (Fig. 14). The largest deviation of the trend of newly formed faults from the alignment parallel to the velocity discontinuity occurred on – or close to – the hanging wall of the reactivated precuts. When the new faults approach the reactivated precuts, they become orthogonal to the precuts themselves, possibly arresting their further propagation (Fig. 14).

3.8. Slip tendency results

Fig. 15 shows the results of the computation of T_s for a variable φ. Notice that the impact of φ is more prominent when the angle between the precuts and the velocity discontinuity is larger. Concerning dip, a value of 30° appears to prevent the precuts from being reused. Since the stress conditions imposed on the analytical model are conservative (i.e., the differential stress is imposed to be tangent to the failure envelope for intact rock, and no pore overpressure is added), the slip tendency value is relatively low ($\leq$0.55). Nonetheless, its variability adequately predicts the precuts behavior in the analog models, yielding the lowermost T_s values for the setups where we observed no reactivation and no anomalies in basin shapes (Table 2). We thus deem that the computation of T_s and our experimental results are in satisfactory agreement.

4. Discussion

Our experimental results showed how the various combinations of precut strike and dip exerted different control on the development and the trajectories of new faults and the shape of new basins. The interaction between new and existing faults depends on the starting orientation of the existing (inherited) faults (precuts) (Fig. 14). Such interaction results in anomalies both in the trajectories of new faults and in the shape of the related basins.

The anomalies in the trajectories of new faults are one of the most interesting results. This behavior was seen in previous studies (e.g., Bellahsen and Daniel, 2005; Deng et al., 2017; Deng et al., 2018; Gudmundsson et al., 2010; Homberg et al., 1997; Maestrelli et al., 2020;

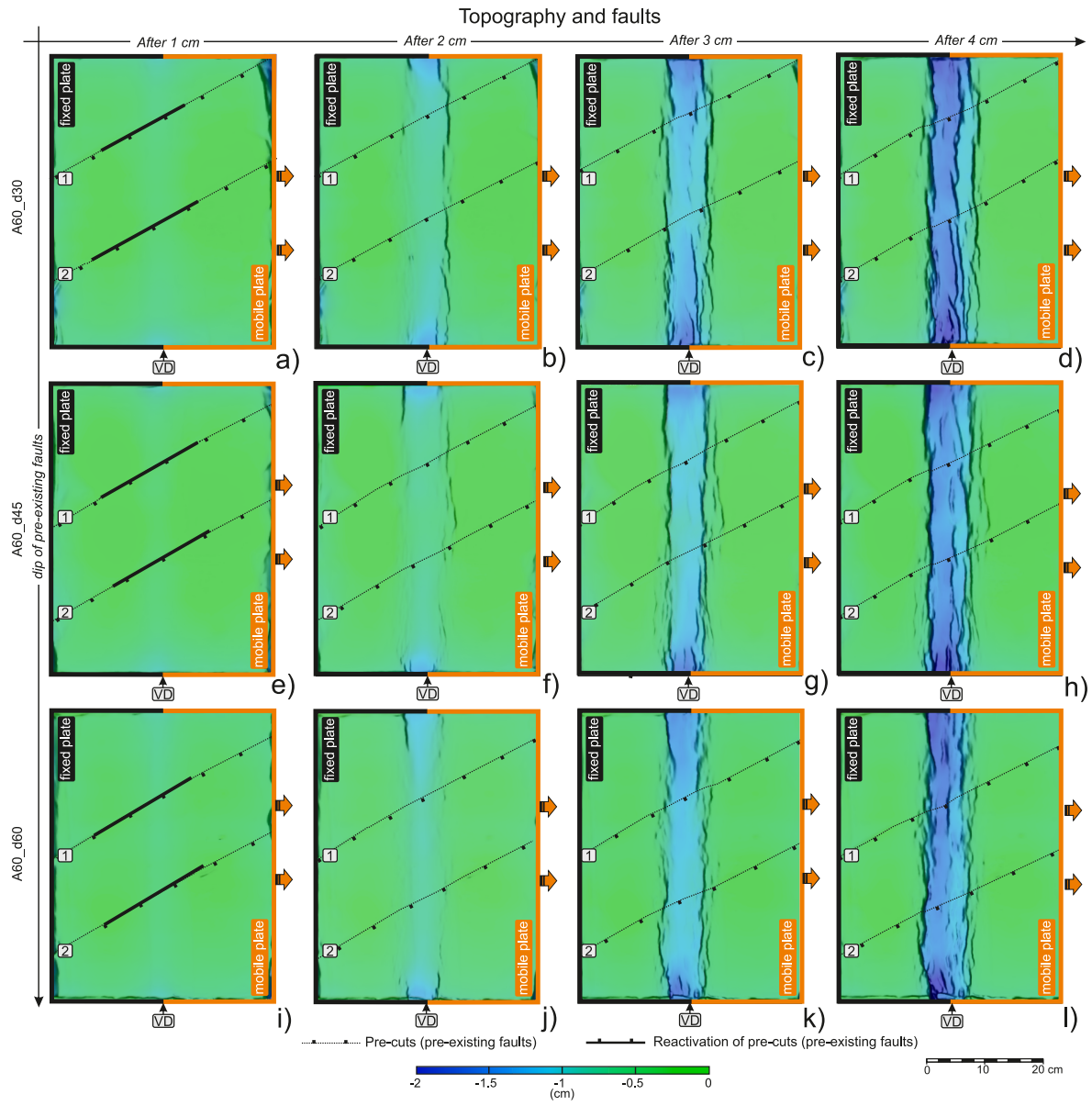

Fig. 9. Free surface of the A60_dxx experiments derived by the digital scan with the color-coded elevation after 1, 2, 3, and 4 cm of base plate displacement. In all panels VD shows the location of the velocity discontinuity. (For interpretation of the references to color in this figure legend, the reader is referred to the Web version of this article.)

Molnar et al., 2019; Osagiede et al., 2021; Willemse, 1997; Zwaan et al., 2021) and is thought to be related to stress reorientation due to slip on an existing mechanical discontinuity (that is, an active pre-existing fault). The same mechanism presumably justifies the broadening or narrowing of the basins, apparently unrelated to an otherwise evident reactivation of the precuts detected on the free surface of the models, as observed by Deng et al. (2017, 2018) in their numerical models. This effect could be due to the interaction of new faults with the precuts at deeper levels of the clay package.

Slip tendency analyses confirmed our modeling results regarding the reactivation of the inherited faults, since both modeling setups were designed to be sensitive to the orientation of inherited faults. Our analog experiments suggest that pre-existing faults striking $\geq 60°$ with respect to the main extensional axis cannot be reactivated. Nevertheless, previous experimental studies demonstrated that faults striking at an even larger angle ($\geq 60°$) might show reactivation (Henza et al., 2010; Bonini et al., 2016). The models shown in these studies and the natural cases recalled bear a major difference with respect to our experiments: they produced non-cylindrical basins with bending from the lateral tip of the emerging faults toward the depocenter. This bending indicates a rotation of the stress axis in the hanging wall of an optimally oriented (and active) extensional fault, implying that an inherited fault that is not optimally oriented relative to the regional stress field may still be reactivated thanks to the local stress field. As reactivation occurs after initiating a new fault, however, the new fault does not show an anomaly in its trajectory (Fig. 16).

The previous discussion suggests that, prior to comparing our results with natural cases, we must always consider all intrinsic limitations of our experiments.

4.1. Modeling limitations

The main limitation of our experimental approach rests in the design of the experimental box. As mentioned in Section 2, there exist different techniques for reproducing extension: since our goals were to obtain a single basin at the center of the box and to analyze how precut segments

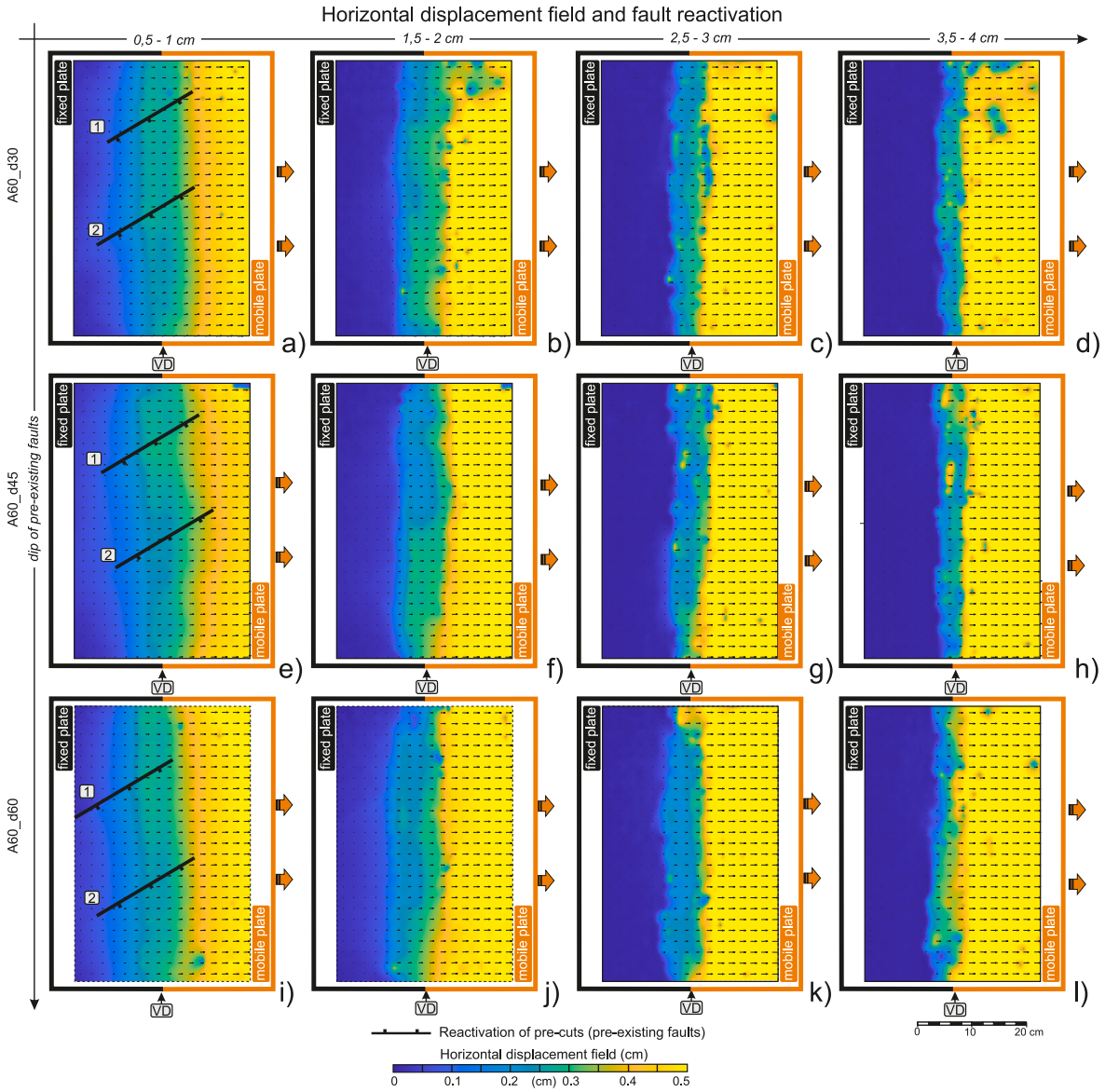

Fig. 10. Incremental displacement field (colors and black arrows) of the A60_dxx experiments computed using D.I.C. (Digital Image Correlation) after 1, 2, 3, and 4 cm of base plate displacement. In all panels VD shows the location of the velocity discontinuity. (For interpretation of the references to color in this figure legend, the reader is referred to the Web version of this article.)

affect any new extensional structures, we selected a setup with a velocity discontinuity at the base of the analog material, As mentioned in the Introduction, over the decades extensional tectonics has been investigated through modeling using different setups (see Zwaan et al., 2019, for a recent discussion of this topic). We may group these studies into two categories, depending on whether they simulate distributed or localized extension. Our setup belongs to the second category, implying that our results cannot be used to discuss the evolution of large-scale tectonic processes, such as the long-term evolution of a rift system, but only smaller-scale deformation processes related to the growth of a single extensional fault and its associated basin.

As previously mentioned, extensional faults are commonly described and investigated using maximum displacement (d_{max}), fault length (L), and the ratio between them (d_{max}/L; e.g., Kim and Sanderson, 2005). The design of our setup produces a quasi-rectilinear fault associated with a cylindrical basin because the velocity discontinuity occurs over a single, discrete and rectilinear feature. The experiment without precuts showed that, at the end of the experiment, the length of the master fault on the left border of the basin was equivalent to the size of the clay cake (Fig. 2j). Over time, the fault trace propagated from the boundaries toward the center of the box due to the different confinement conditions (down to zero) near the free edges of the model. These observations indicate that we could not use the evolution of the fault length to discuss theoretical studies and natural cases because the growth of a normal fault initiates from a point and grows laterally (e.g., Cowie and Scholz, 1992; Burgmann et al., 1994; Childs et al., 2003).

We thus used the length and d_{max} measured along the reactivated precuts as a qualitative proxy to summarize our results and highlight the differences between cut and uncut models. The reactivation of the precuts was observed in every experiment (Figs. 3–12). We refrained from a quantitative analysis of the reactivation length, however, given its dependence on the portion of the precuts located in the central extensional area which varies with their strike.

4.2. Natural examples

To complement our results and the cases we explored with our models, we analyzed three natural cases showing examples of how

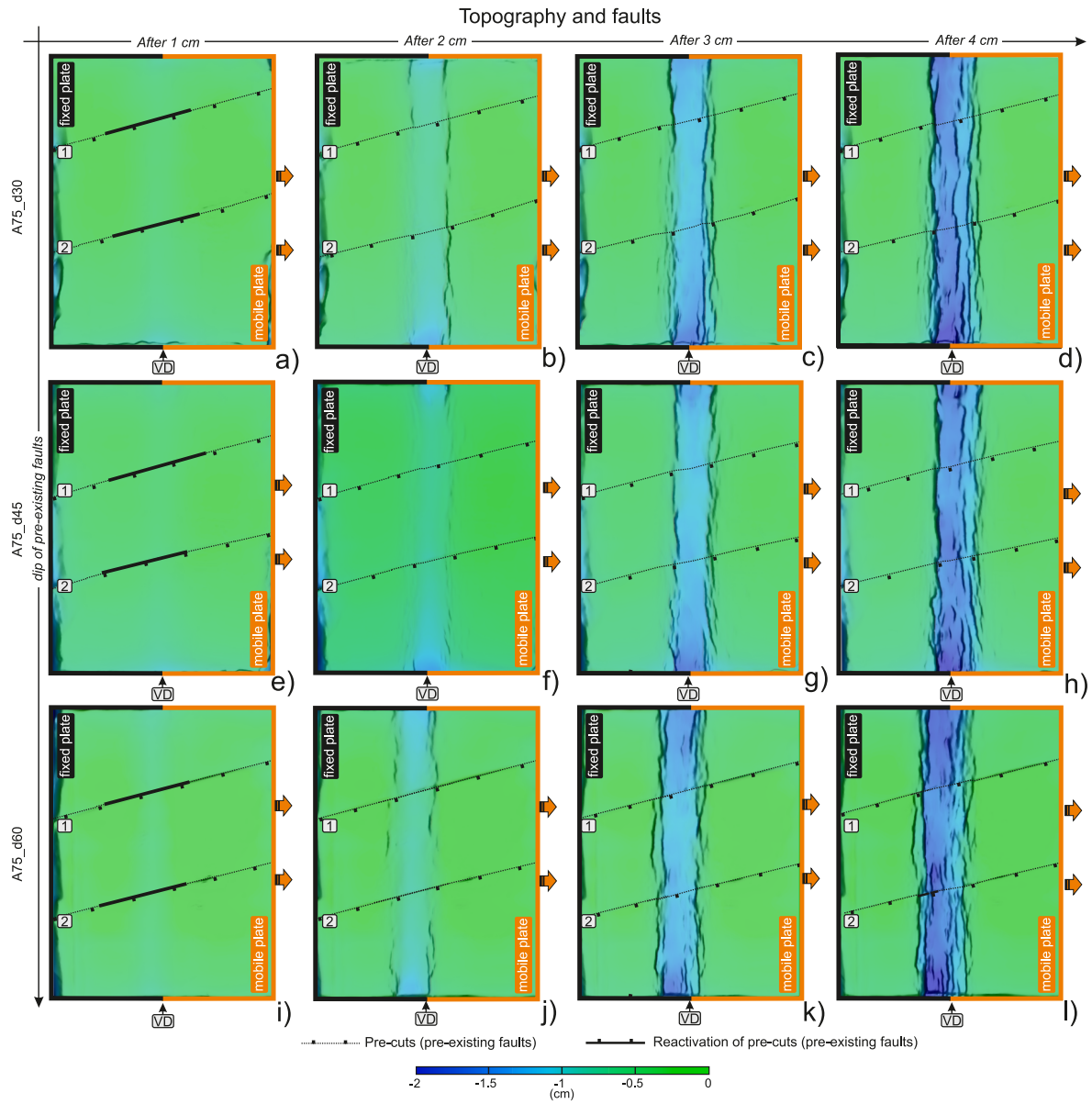

Fig. 11. Free surface of the A75_dxx experiments derived by the digital scan with the color-coded elevation after 1, 2, 3, and 4 cm of base plate displacement. Top-view sketch summary of experimental results. In all panels VD shows the location of the velocity discontinuity. (For interpretation of the references to color in this figure legend, the reader is referred to the Web version of this article.)

inherited structures affect the subsequent evolution of new extensional faults.

The first case concerns the Tusse Fault, located offshore Norway; it represents a multiple-rifted area, where diachronous and variously oriented extensional faults formed complex basins (Fig. 17a and b). These basins derive both from a Late Permian-to-Early Triassic and a Late Jurassic-to-Early Cretaceous rifting phases (e.g., Whipp et al., 2014; Duffy et al., 2015). Among different examples of interactions between older and younger faults, the present-day setting of the Tusse Fault is reminiscent of one of our experimental findings (Fig. 17b, c, and e). A trajectory anomaly occurs when the Tusse Fault interacts with an older extensional fault (Fault 1 in Fig. 17 b, c), showing the same behavior of the newly formed faults we found in A30_d60 (Fig. 17d). Another anomaly is seen in the corresponding basin shape, which shows a broadening in the hanging wall of the older fault (Fault 1) and a narrowing in its footwall (Fig. 11c and d). Such geometry implies that the older fault (Fault 1) was still active during the activity and growth of the Tusse Fault.

The second case concerns Central Italy, where present-day extension follows a contractional regime, implying that new extensional faults developed in a region where numerous relatively low-angle faults already existed (Fig. 17f and g). The example concerns an area hit by a severe earthquake sequence in 2016–17, when two M $\geq$ 6 events devastated a large area of the Central Apennines (e.g., Michele et al., 2016). The M 6.5 October 30, 2016 Norcia earthquake, the largest shock of the sequence, documented the present-day extensional reactivation of an inherited ~35°-dipping large thrust and of a set of high-angle secondary faults both in its hanging wall and footwall (e.g., Bonini et al., 2019; Buttinelli et al., 2021; Di Bucci et al., 2021, Fig. 16f, g, h). The strike difference between thrust and extensional faults is about 30°. The anomaly in the general trend of the extensional faults cutting the hanging wall and footwall of the negatively reactivated thrust is quite similar to that shown in our A30_d30 (Fig. 16i and j). In the modeling case, the partial reactivation of a low-angle precut controlled the trend of new faults and the shape of the associated basin. This result confirms previous findings showing that the interaction between the present-day

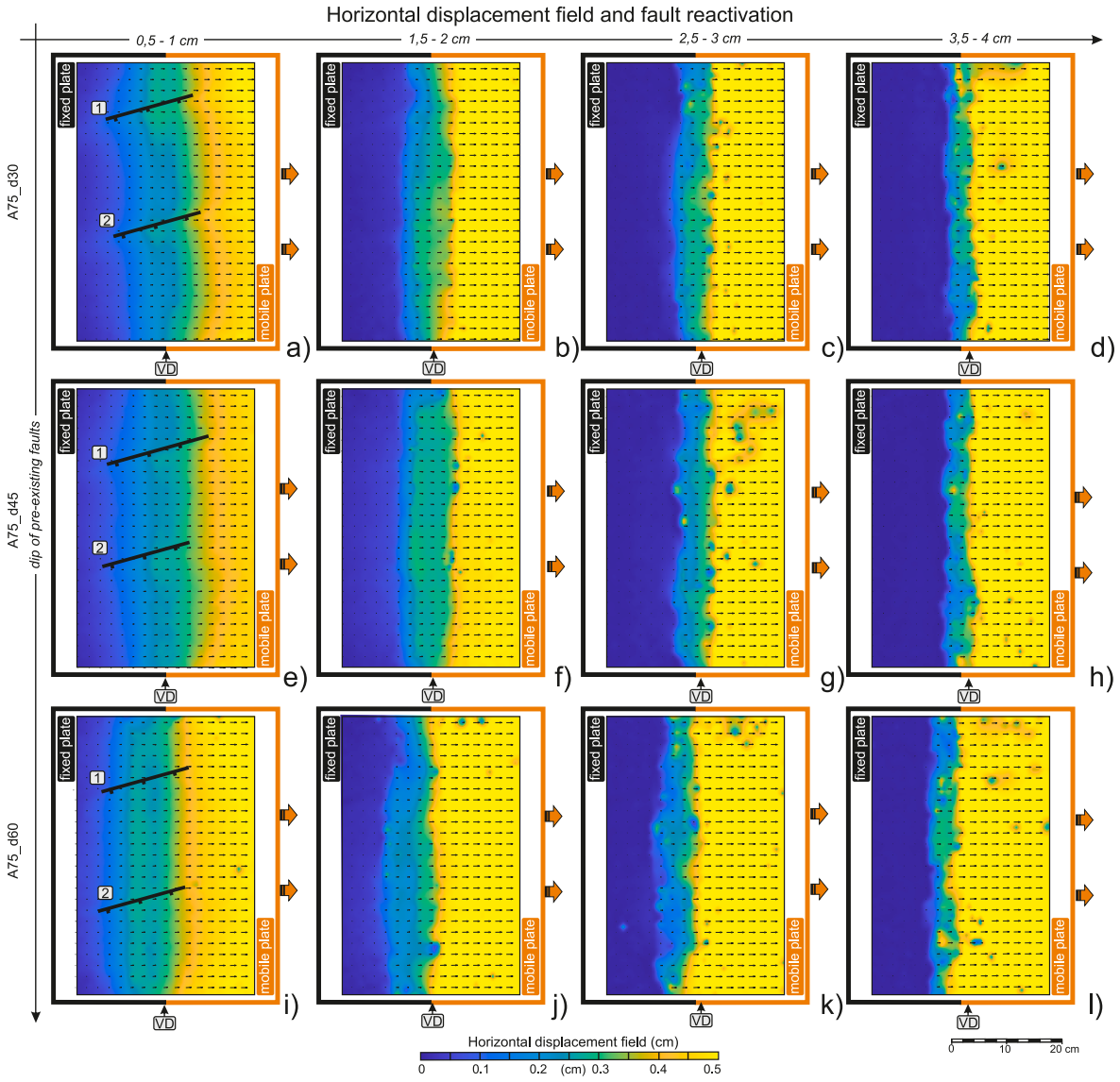

Fig. 12. Incremental displacement field (colors and black arrows) of the A60_dxx experiments computed using D.I.C. (Digital Image Correlation) after 1, 2, 3, and 4 cm of base plate displacement. In all panels VD shows the location of the velocity discontinuity. (For interpretation of the references to color in this figure legend, the reader is referred to the Web version of this article.)

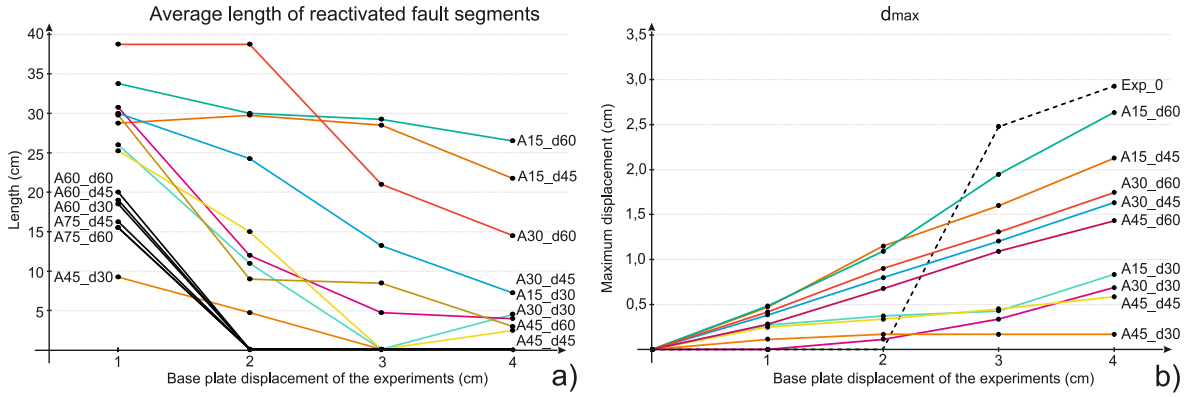

Fig. 13. a) Average length of reactivated precut segments, detected using anomalies in the displacement field computed using D.I.C. (Digital Image Correlation) after 1, 2, 3, and 4 cm of base plate displacement. B) Average maximum displacement (d_{max}) measured along the precuts after 1, 2, 3, and 4 cm of base plate displacement. Both diagrams show results only of the experiments where reactivation was observed.

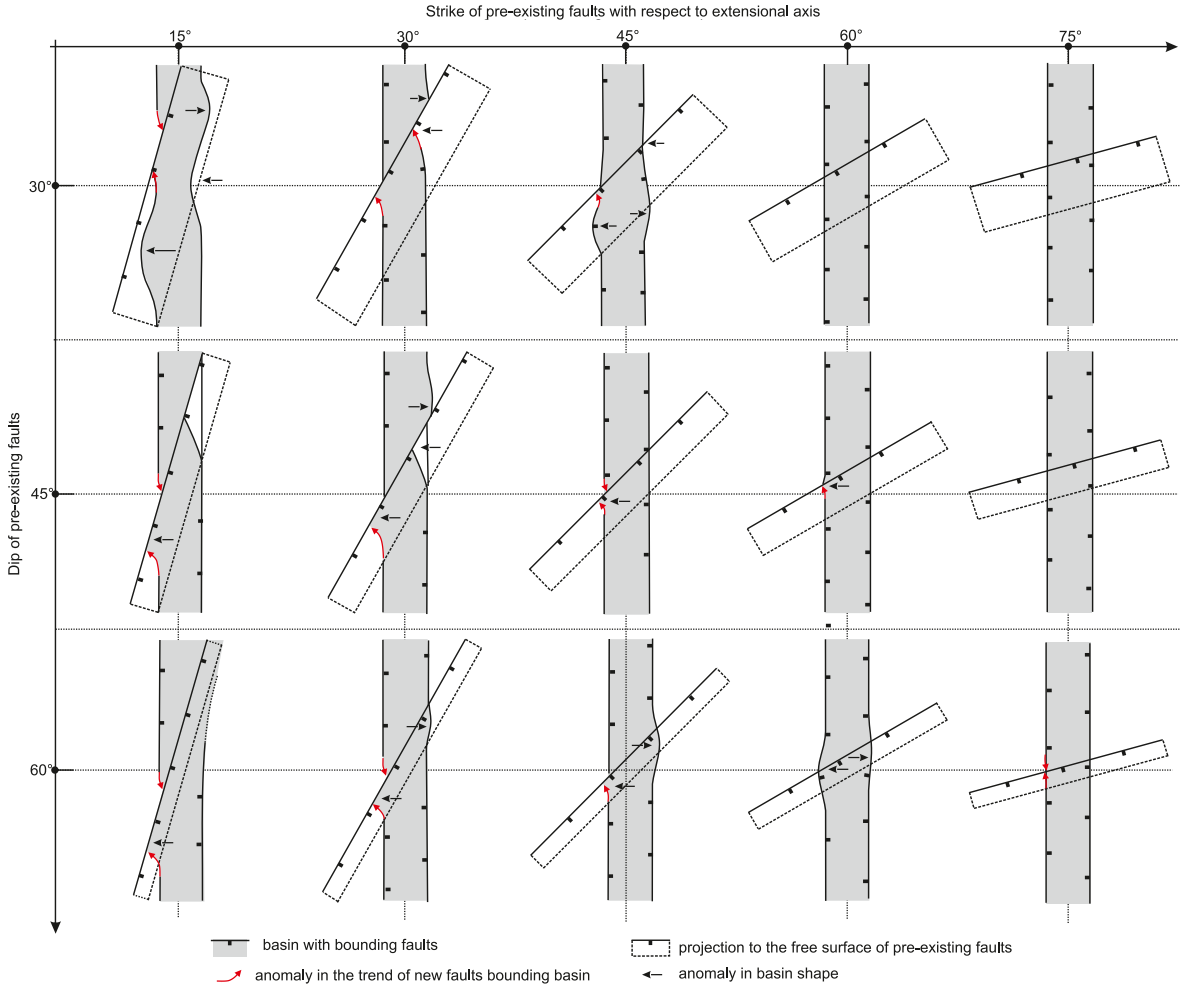

Fig. 14. Top-view sketch summary of experimental results.

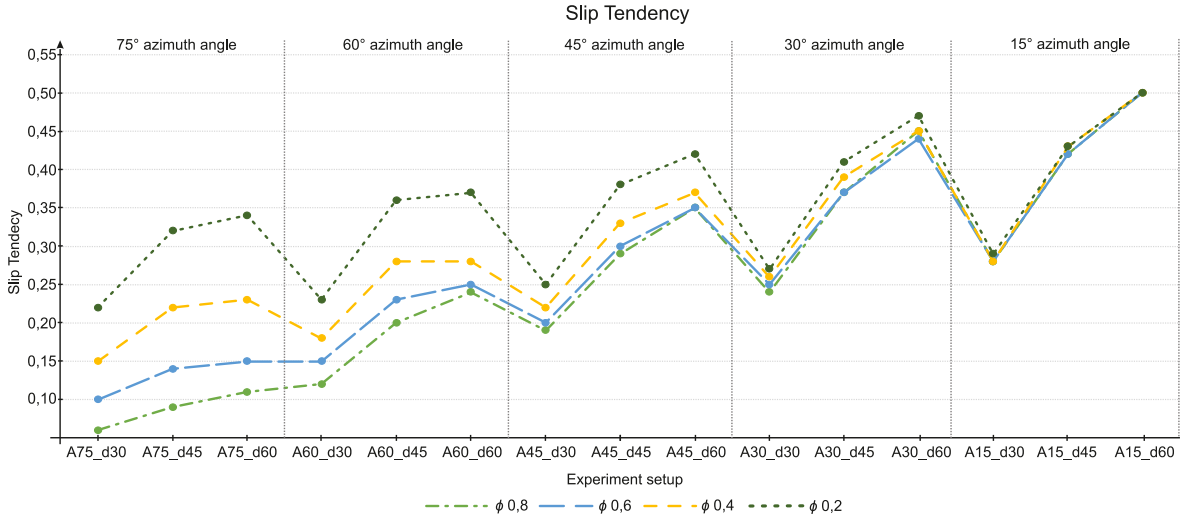

Fig. 15. Results of the slip-tendency analysis for varying φ (shape of the stress ellipsoid), conducted on faults having the same geometry (dip and strike) as those in the analog experiments.

extensional stress field and the inherited compressional structures may control the activity of Quaternary fault systems (Del Ventisette et al., 2021).

The third case concerns the East African Rift System, a nearly 5000-km-long, multiple-branched extensional fault system that separates the African Plate from the Somali Plate (Fig. 18a). The most recent extensional structures developed mainly since the Oligo-Miocene (e.g., Morley, 1999; Michon et al., 2022), but the region underwent several

Table 2
Results from the slip-tendency (T_s) analysis for different setups, and comparison with analog modeling results.

Setup	Strike (°)	Dip (°)	Precut Reactivation in analogue models	Basin shape anomaly in analog models	Ts φ 0.8	Ts φ 0.6	Ts φ 0.4	Ts φ 0.2
A75_d30	75	30	No	No	0.11	0.15	0.20	0.27
A75_d45	75	45	only in the early phase	No	0.14	0.19	0.27	0.37
A60_d30	60	30	only in the early phase	No	0.17	0.20	0.23	0.28
A75_d60	75	60	only in the early phase	Yes	0.16	0.20	0.28	0.39
A45_d30	45	30	Yes	Yes	0.24	0.25	0.27	0.30
A60_d45	60	45	only in the early phase	Yes	0.25	0.28	0.33	0.41
A60_d60	60	60	only in the early phase	Yes	0.29	0.30	0.33	0.42
A30_d30	30	30	Yes	Yes	0.29	0.30	0.31	0.32
A15_d30	15	30	Yes	Yes	0.33	0.33	0.33	0.34
A45_d45	45	45	Yes	Yes	0.34	0.35	0.38	0.43
A45_d60	45	60	Yes	Yes	0.40	0.40	0.42	0.47
A30_d45	30	45	Yes	Yes	0.42	0.42	0.44	0.46
A15_d45	15	45	Yes	Yes	0.47	0.47	0.48	0.48
A30_d60	30	60	Yes	Yes	0.50	0.49	0.50	0.52
A15_d60	15	60	Yes	Yes	0.55	0.55	0.55	0.55

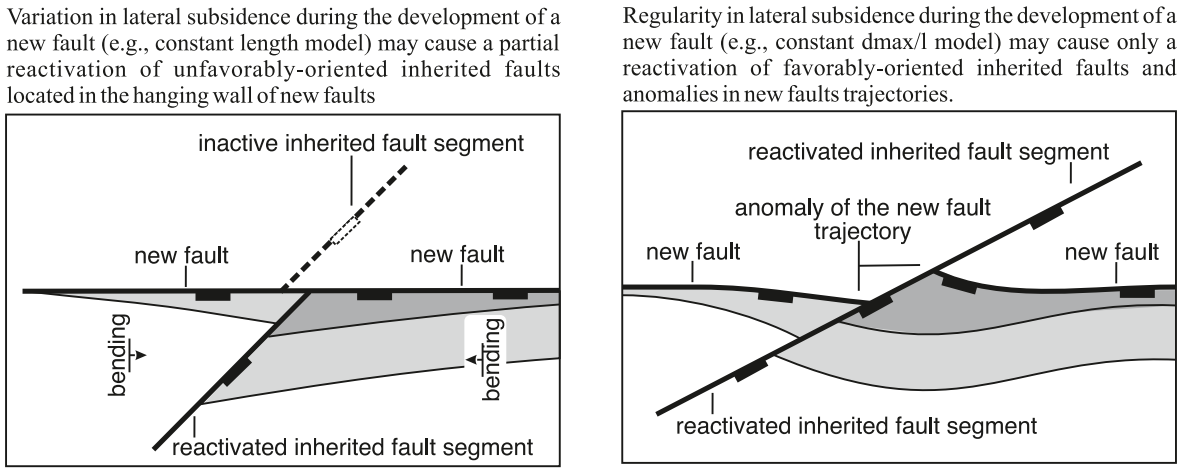

Fig. 16. Idealized evolution of a new extensional fault with partial (left panel) and full reactivation (right panel) of an inherited fault and its effect on the evolution of the basin shape. Dark gray indicates the deeper part of the basins.

extensional phases before the Eocene (e.g., Macgregor, 2018). The Rukwa-North Malawi segment represents an oblique linkage between the Western and Southern branches (e.g., Heilman et al., 2019). The present-day structural setting of Rukwa Rift consists of multiple NNW-trending fault systems associated with different extensional phases, from the Permo-Triassic (e.g., Delvaux, 2001) and Cretaceous (e.g., Roberts et al., 2010) to Cenozoic rifting (e.g., Morley, 1999; Delvaux, 2001). The Rukwa Rift basin is bounded by the Lupa Fault to the northeast and the Ufipa Fault to the southwest (Fig. 18b). Recent seismicity suggests pure normal faulting due to rotation of the local stress field (e.g., Morley et al., 2004; Kolawole et al., 2021). In the northernmost part of the Rukwa Rift basin, the Ufipa Fault terminates at a high angle against the inherited WNW-ESE Chisi Shear Zone (Fig. 18c) and forms a basin-ward salient (e.g., Heilman et al., 2019). The Chisi Shear Zone represents a major suture between the Tanzania Craton and the Bangweulu Block (e.g., Lemna et al., 2019). Several studies suggest an active role of this suture zone in the development of extensional faulting over southern Tanzania and northern Malawi (e.g., Morley, 1999; Delvaux, 2001; Lemna et al., 2019). The strike difference between the main trend of the Ufipa Fault and the Chisi Shear Zone in the northern Rukwa Rift is about 30°. Following our experimental results (Fig. 18d and e), the anomaly in the trend of the Ufipa Fault close to the Chisi Shear Zone suggests that these two structures were both active during the development of the Rukwa Rift basin.

5. Conclusions

We ran a large set of analog experiments to test if and how the equivalent of inherited dip-slip faults (precuts) forming an angle with the trend of an extensional stress field impacts the evolution of new extensional faults and their associated basins. We specifically focused on the geometry and distribution of newly incepted faults resulting from incremental deformation applied to precuts with different orientations (from 15° to 75° relative to the strike of extension) and dips (from 30° to 60°). We then analyzed if and how differently oriented pre-existing faults affect the evolution of an extensional basin.

Our results show that when strike and dip of pre-existing faults are very close to those of an optimally oriented extensional fault, their influence on the development of the resulting extensional basin is more significant. This finding applies also to the trend of newly formed faults and the resulting basin shape.

As for the trend of newly formed faults, their trajectories exhibit an anomaly when new and pre-existing faults are active simultaneously. The interaction between reactivated and new faults induces anomalies also in the spatial arrangement and geometry of the associated basin, whose cylindrical development either broadens or narrows if compared to what is expected in an ideal scenario, i.e., a setup in which a basin develops within an isotropic and homogeneous succession.

The structural anomalies observed in natural test cases support our experimental results. In the first case, located offshore Norway, the trend of many recent extensional faults exhibits anomalies in areas dissected

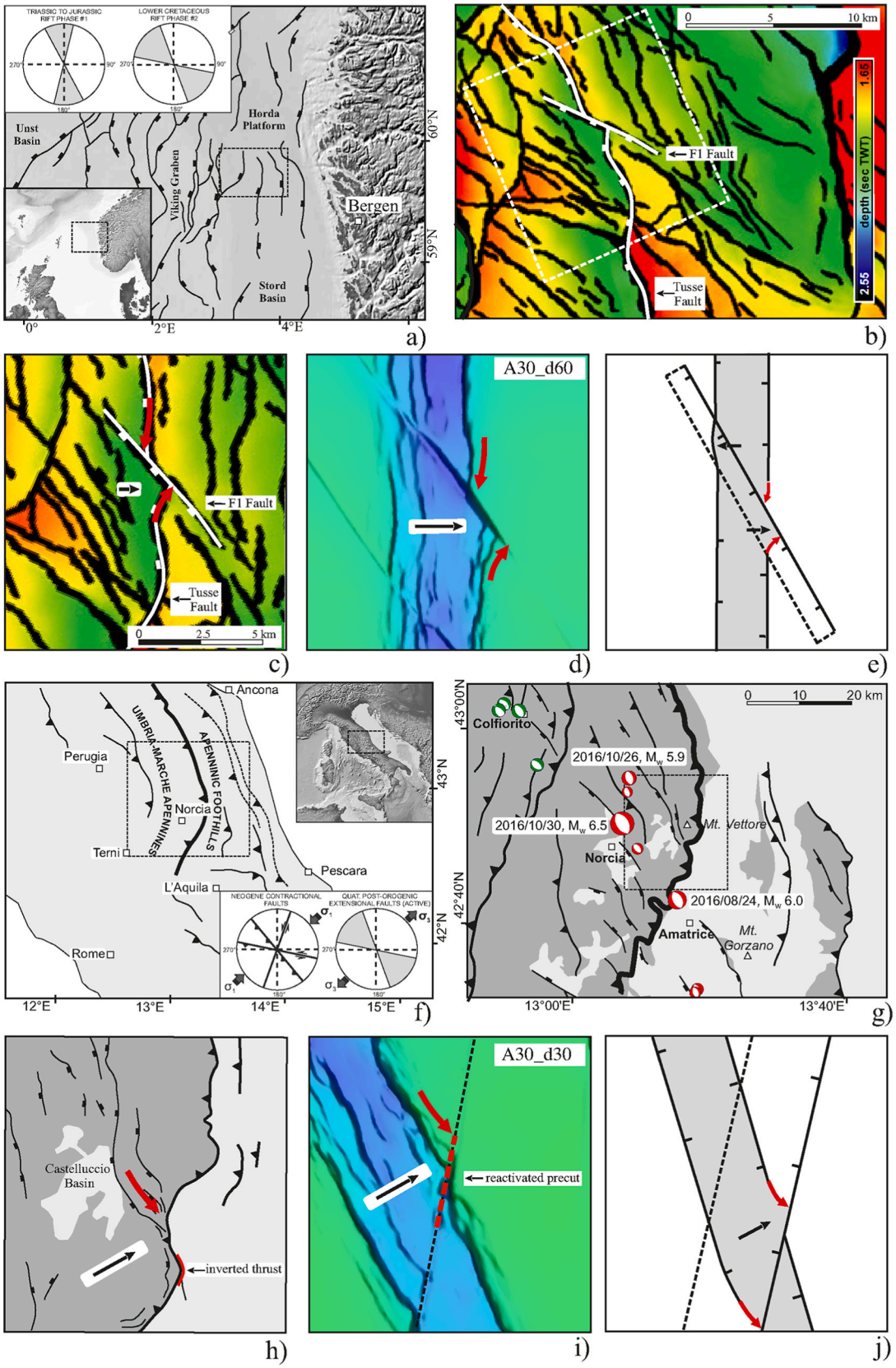

Fig. 17. Tectonic sketch maps of natural examples (a, b, c, f, g, h); excerpts from our experiments (d, i) and summary of Fig. 14 (e, j). a), b), c) Tectonic map of the Horda Platform in the North Sea (a); close-up of the area crossed by the Tusse Fault (b and c; modified from Whipp et al., 2014). f), g), and h) Tectonic map of central Italy; thick black lines in f) and g) show the Sibillini Thrust system. In all panels, red and black arrows mark the anomalies in the trend of newly-incepted faults and the spatial arrangement of their associated basins, respectively. Notice that for ease of comparison with the natural examples, experiments and panels from Fig. 14 are shown overturned with respect to other figures. (For interpretation of the references to color in this figure legend, the reader is referred to the Web version of this article.)

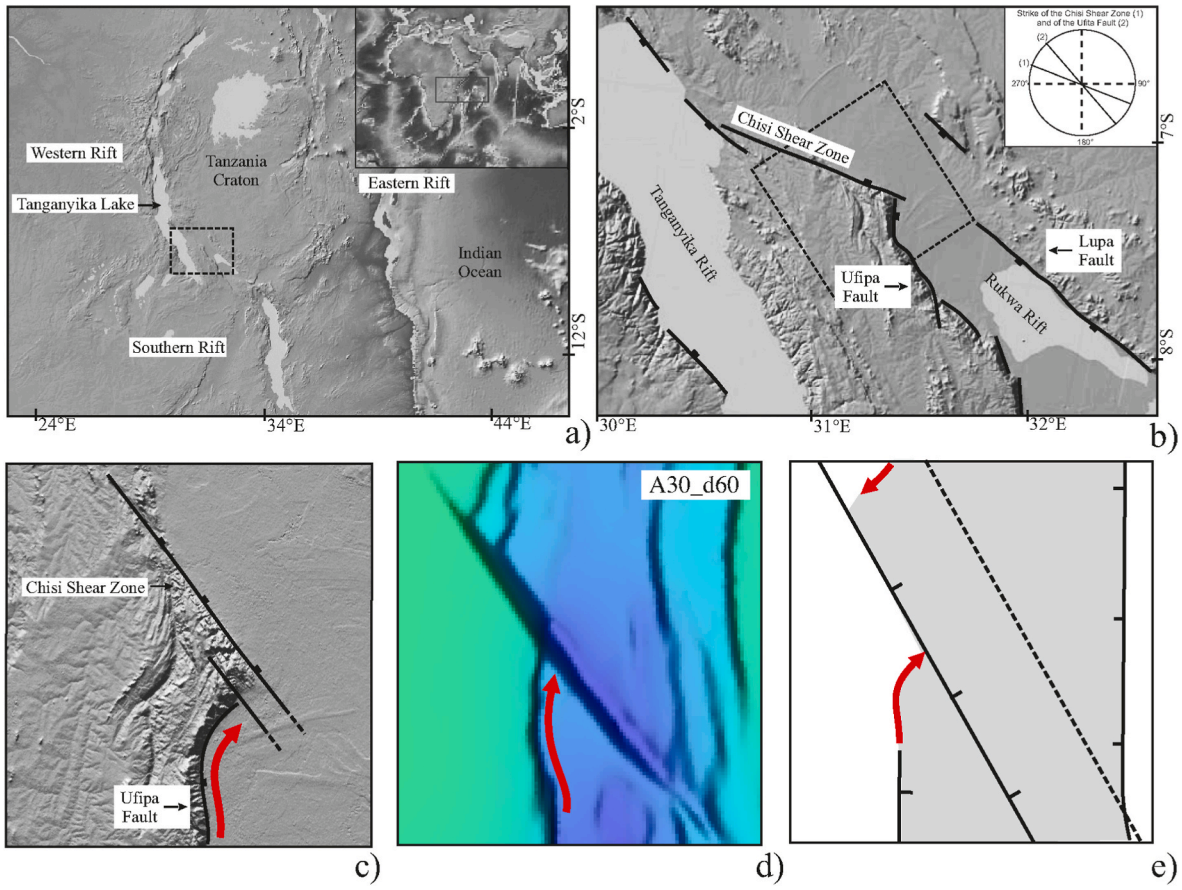

Fig. 18. Simplified map of the East African Rift System. b) Map of main faults between Rukwa and Tanganyika rifts (after Lavayssière et al., 2019). c) Close-up of the interaction between the Ufipa Fault and Chisi Shear Zone (modified from Kolawole et al., 2021). d) Close-up of the A30_d60 experiment and e) of the related panel in Fig. 14. Red arrows in panels c), d), and f) represent the anomalies in the trend of newly-incepted faults. Notice that for ease of comparison with natural examples, the experiment and the panel from Fig. 14 are overturned with respect to other figures. (For interpretation of the references to color in this figure legend, the reader is referred to the Web version of this article.)

by faults inherited from a previous extensional phase. Anomalies in fault trends have been suggested for another natural test case in Central Italy, where active Quaternary extensional faults interact with thrust faults inherited from a mountain building phase. The same mechanism has been observed in the Rukwa Rifts (East Africa Rift System), where the trend of a recent fault has been deflected by the reactivation of an ancient shear zone.

When investigating areas whose evolution is likely affected by faults inherited from older tectonic phases, our findings can be used to decipher anomalies in the trend of the most recent extensional fault systems and in the 3D geometry of their associated basins.

Author statement

Lorenzo Bonini: Conceptualization; Data curation; Formal analysis; F Investigation; Methodology; Project administration; Resources; Software; Validation; Visualization; Roles/Writing - original draft. **Umberto Fracassi**: Conceptualization; Data curation; Funding acquisition; Investigation; Methodology; Resources; Supervision; Validation; Visualization; Writing - review & editing. **Nicolò Bertone**: Conceptualization; Data curation; Formal analysis; F Investigation; Methodology; Software; Validation; Visualization; Writing - review & editing. **Francesco Emanuele Maesano**: Conceptualization; Data curation; Formal analysis; F Investigation; Methodology; Software; Validation; Visualization; Writing - review & editing. **Gianluca Valensise**: Conceptualization; Funding acquisition; Investigation; Methodology; Supervision; Validation; Visualization; Writing - review & editing. **Roberto Basili**: Conceptualization; Data curation; Funding acquisition; Investigation; Methodology; Resources; Supervision; Validation; Visualization; Writing - review & editing.

Declaration of competing interest

The authors declare that they have no known competing financial interests or personal relationships that could have appeared to influence the work reported in this paper.

Data availability

Data will be made available on request.

Acknowledgments

Part of this work was funded by the project "The impact of an inherited structural setting on the development of extensional systems in the Amatrice-Norcia-Visso area: insights from analog modeling" (UR 0865.050; P.I.: Umberto Fracassi), part of the INGV-FISR 2016 Project - Italia centrale "*Centro di studio e monitoraggio dei rischi naturali dell'Italia centrale*" (cod. D82F16001180001), and by the INGV "FASTMIT" Project (UR 0850.010; P.I.: Roberto Basili – cod. D52F16001150001). The editor Jianhua Li and the reviewers Laurent Michon and Frank Zwaan are gratefully acknowledged for improving the quality of this paper through their reviews and constructive criticism.

Appendix ASupplementary data

Supplementary data to this article can be found online at https://doi.org/10.1016/j.jsg.2023.104836.

References

Aanyu, K., Koehn, D., 2011. Influence of pre-existing fabrics on fault kinematics and rift geometry of interacting segments: analogue models based on the Albertine Rift (Uganda), Western Branch-East African Rift System. J. Afr. Earth Sci. 59 (2–3), 168–184.

Anderson, E.M., 1951. The Dynamics of Faulting and Dyke Formation with Application to Britain, second ed. Oliver and Boyd, Edinburgh, p. 206.

Autin, J., Bellahsen, N., Leroy, S., Husson, L., Beslier, M.-O., d'Acremont, E., 2013. The role of structural inheritance in oblique rifting: insights from analogue models and application to the gulf of aden. Tectonophysics 607, 51–64. https://doi.org/10.1016/j.tecto.2013.05.041.

Angelier, J., 1979. Determination of the mean principal directions of stresses for a given fault population. Tectonophysics 56, T17–T26.

Bell, R.E., Jackson, C.A.L., Whipp, P.S., 2014. Strain migration during multiphase extension: observations from the northern North Sea. Tectonics 33 (10), 1936–1963.

Bellahsen, N., Daniel, J.M., 2005. Fault reactivation control on normal fault growth: an experimental study. J. Struct. Geol. 27 (4), 769–780. https://doi.org/10.1016/j.jsg.2004.12.003.

Bonanno, E., Bonini, L., Basili, R., Toscani, G., Seno, S., 2017. How do horizontal, frictional discontinuities affect reverse fault- propagation folding? J. Struct. Geol. 102, 147–167.

Bonini, L., Basili, R., Burrato, P., Cannelli, V., Fracassi, U., Maesano, F.E., Melini, D., Tarabusi, G., Tiberti, M.M., Vannoli, P., Valensise, G., 2019. Testing different tectonic models for the source of the Mw 6.5 October 2016, Norcia Earthquake (Central Italy): a youthful normal fault, or negative inversion of an old thrust? Tectonics 38. https://doi.org/10.1029/2018TC005185.

Bonini, L., Basili, R., Toscani, G., Burrato, P., Seno, S., Valensise, G., 2015. The role of preexisting discontinuities in the development of extensional faults: an analog modeling perspective. J. Struct. Geol. 74, 145–158. https://doi.org/10.1016/j.jsg.2015.03.004.

Bonini, L., Basili, R., Toscani, G., Burrato, P., Seno, S., Valensise, G., 2016. The effects of pre-existing discontinuities on the surface expression of normal faults: insights from wet clay analog modeling. Tectonophysics. https://doi.org/10.1016/j.tecto.2015.12.015.

Bonini, L., Di Bucci, D., Toscani, G., Seno, S., Valensise, G., 2014. On the complexity of surface ruptures during normal faulting earthquakes: excerpts from the 6 April 2009 L'Aquila (Central Italy) earthquake (Mw 6.3). Solid Earth 5, 389–408. https://doi.org/10.5194/se-5-389-2014.

Bonini, M., Souriot, T., Boccaletti, M., Brun, J.P., 1997. Successive orthogonal and oblique extension episodes in a rift zone: laboratory experiments with application to the Ethiopian Rift. Tectonics 16 (2), 347–362. https://doi.org/10.1029/96tc03935.

Bramham, E.K., Wright, T.J., Paton, D.A., Hodgson, D.M., 2021. A new model for the growth of normal faults developed above pre-existing structures. Geology. https://doi.org/10.1130/G48290.1.

Buttinelli, M., Petracchini, L., Maesano, F.E., D'Ambrogi, C., Scrocca, D., Marino, M., Capotorti, F., Bigi, S., Cavinato, G.P., Mariucci, M.T., Montone, P., Di Bucci, D., 2021. The impact of structural complexity, fault segmentation, and reactivation on seismotectonics: constraints from the upper crust of the 2016-2017 Central Italy seismic sequence area. Tectonophysics 810. https://doi.org/10.1016/j.tecto.2021.228861.

Burgmann, R., Pollard, D.D., Martel, S.J., 1994. Slip distributions on faults: effects of stress gradients, inelastic deformation, heterogeneous host-rock stiffness, and fault interaction. J. Struct. Geol. 16, 1675–1690.

Byerlee, J., 1978. Friction of rocks. Pure Appl. Geophys. 116, 615–626.

Childs, C., Nicol, A., Walsh, J.J., Watterson, J., 2003. The growth and propagation of synsedimentary faults. J. Struct. Geol. 25, 633–648.

Claringbould, J.S., Bell, R.E., Jackson, C.A.-L., Gawthorpe, R.L., Odinsen, T., 2017. Pre-existing normal faults have limited control on the rift geometry of the northern North Sea. Earth Planet Sci. Lett. 475, 190–206.

Cloos, E., 1968. Experimental analysis of Gulf Coast fracture patterns. AAPG (Am. Assoc. Pet. Geol.) Bull. 52, 420–444.

Collanega, L., Siuda, K., Jackson, C.A.L., Bell, R.E., Coleman, A.J., Lenhart, A., et al., 2019. Normal fault growth influenced by basement fabrics: the importance of preferential nucleation from pre-existing structures. Basin Res. 31, 659–687.

Collettini, C., Sibson, R.H., 2001. Normal faults, normal friction? Geology 29 (10), 927e930. https://doi.org/10.1130/0091-7613.

Cooke, M.L., Schottenfeld, M.T., Buchanan, S.W., 2013. Evolution of fault efficiency at restraining bends within wet kaolin analog experiments. J. Struct. Geol. 51, 180–192.

Cooke, M.L., van der Elst, N.J., 2012. Rheologic testing of wet kaolin reveals frictional and bi-viscous behavior typical of crustal materials. Geophys. Res. Lett. 39 https://doi.org/10.1029/2011GL050186.

Corti, G., 2009. Continental rift evolution: from rift initiation to incipient break-up in the Main Ethiopian Rift, East Africa. Earth Sci. Rev. 96 (1–2), 1–53.

Corti, G., Molin, P., Sembroni, A., Bastow, I.D., Keir, D., 2018. Control of pre-rift lithospheric structure on the architecture and evolution of continental rifts: insights from the Main Ethiopian Rift, East Africa. Tectonics 37, 477–496. https://doi.org/10.1002/2017TC004799.

Corti, G., Maestrelli, D., Sani, F., 2022. Large-to local-scale control of pre-existing structures on continental rifting: examples from the main Ethiopian rift, east Africa. Front. Earth Sci. 10 https://doi.org/10.3389/feart.2022.808503.

Cowie, P.A., Scholz, C.H., 1992. Physical explanation for the displacement–length relationship for faults using a post-yield fracture mechanics model. J. Struct. Geol. 14, 1133–1148.

Del Ventisette, C., Bonini, M., Maestrelli, D., Sani, F., Iavarone, E., Montanari, D., 2021. 3D-thurst fault pattern control on negative inversion: an analogue modelling perspective on central Italy. J. Struct. Geol. 143, 104254 https://doi.org/10.1016/j.jsg.2020.104254.

Delvaux, D., 2001. Tectonic and palaeostress evolution of the tanganyika-rukwa-Malawi rift segment, East African Rift System. In: Ziegler, P.A., Cavazza, W., Robertson, A.H. F. (Eds.), PeriTethyan Rift/Wrench Basis and Passive MarginsPeri-Tethys Memoir, vol. 186. Mem. Natn. Hist. nat, Paris, pp. 545–567, 6.

Deng, C., Gawthorpe, R.L., Finch, E., Fossen, H., 2017. Influence of a pre-existing basement weakness on normal fault growth during oblique extension: insights from discrete element modeling. J. Struct. Geol. 105, 44–61.

Deng, C., Gawthorpe, R.L., Fossen, H., Finch, E., 2018. How does the orientation of a preexisting basement weakness influence fault development during renewed rifting? Insights from three-dimensional discrete element modeling. Tectonics 37 (7–8), 2221–2242.

Di Bucci, et al., 2021. RETRACE-3D project: a multidisciplinary collaboration to build a crustal model for the 2016-2018 central Italy seismic sequence. Bollettino di Geofisica Teorica ed Applicata. https://doi.org/10.4430/bgta0343.

Duclaux, G., Huismans, R.S., May, D.A., 2020. Rotation, narrowing, and preferential reactivation of brittle structures during oblique rifting. Earth Planet Sci. Lett. 531, 115952.

Duffy, O.B., Bell, R.E., Jackson, C.A.-L., Gawthorpe, R.L., Whipp, P.S., 2015. Fault growth and interactions in a multiphase rift fault network: Horda Platform, Norwegian North Sea. J. Struct. Geol. 80, 99–119.

Eisenstadt, G., Sims, D., 2005. Evaluating sand and clay models; do rheological differences matter? J. Struct. Geol. 27, 1399–1412.

Eisenstadt, G., Withjack, M.O., 1995. Estimating inversion: results from clay models. In: BUCHANAN, J.G., BUCHANAN, P.G. (Eds.), Basin Inversion, vol. 88. Geological Society Special Publication, pp. 119–136, 1995, 88, 119-136.

Fedorik, J., Toscani, G., Lodolo, E., Civile, D., Bonini, L., Seno, S., 2018. Structural analysis and miocene-to-present tectonic evolution of a lithosphere-scale, transcurrent lineament: the sciacca fault (Sicilian channel, central mediterranean Sea). Tectonophysics 722, 342–355.

Fjær, E., Ruistuen, H., 2002. Impact of the intermediate principal stress on the strength of the heterogeneous rock. J. Geophys. Res. Solid Earth. https://doi.org/10.1029/2001JB000277.

Frankowicz, E., Mcclay, K.R., 2010. Extensional fault segmentation and linkages, Bonaparte Basin, outer North West shelf, Australia. AAPG (Am. Assoc. Pet. Geol.) Bull. 94 (7), 977–1010.

Gudmundsson, A., Simmenes, T.H., Larsen, B., Philipp, S.L., 2010. Effects of internal structure and local stresses on fracture propagation, deflection, and arrest in fault zones. J. Struct. Geol. 32, 1643–1655.

Handin, 1966. Strength and ductility. In: Clark, S.P. (Ed.), Handbook of Physical Constants, 97. Geological Society of America Memoir, pp. 233–289.

Hatem, A.E., Cooke, M.L., Toeneboehn, K., 2017. Strain localization and evolving kinematic efficiency of initiating strike-slip faults within wet kaolin experiments. J. Struct. Geol. 101, 96–108.

Hatem, A.E., Cooke, M.L., Madden, E.H., 2015. Evolving efficiency of restraining bends within wet kaolin analog experiments. J. Geophys. Res. Solid Earth 120 (3), 1975–1992.

Heilman, E., Kolawole, F., Atekwana, E.A., Mayle, M., 2019. Controls of basement fabric on the linkage of rift segments. Tectonics 38, 1337–1366. https://doi.org/10.1029/2018TC005362.

Hempton, M., Neher, K., 1986. Experimental fracture, strain and subsidence patterns over en echelon strike-slip faults: implications for the structural evolution of pull-apart basins. J. Struct. Geol. 8, 597–605.

Henstra, G.A., Berg Kristensen, T., Rotevatn, A., Gawthorpe, R.L., 2019. How do pre-existing normal faults influence rift geometry? A comparison of adjacent basins with contrasting underlying structure on the Lofoten Margin, Norway. Basin Res. 31 (6), 1083–1097.

Henza, A.A., Withjack, M.O., Schlische, R.W., 2010. Normal-fault development during two phases of non-coaxial extension: an experimental study. J. Struct. Geol. 32, 1656–1667.

Homberg, C., Hu, J.C., Angelier, J., Bergerat, F., Lacombe, O., 1997. Characterization of stress perturbations near major fault zones: insights from 2-D distinct-element numerical modelling and field studies (Jura mountains). J. Struct. Geol. 19 (5), 703–718.

Hubbert, M.K., 1937. Theory of scale models as applied to the study of geologic structures. Geol. Soc. Am. Bull. 48, 1459e1520.

Jackson, J.A., White, N.J., 1989. Normal faulting in upper continental crust: observations from regions of active extension. J. Struct. Geol. 11, 15e36.

Keep, M., McClay, K.R., 1997. Analogue modelling of multiphase rift systems. Tectonophysics 273, 239–270. https://doi.org/10.1016/S0040-1951(96)00272-7.

Kim, Y.-S., Sanderson, D.J., 2005. The relationship between displacement and length of faults: a review. Earth Sci. Rev. 68, 317–334.

Kolawole, F., Phillips, T.B., Atekwana, E.A., Jackson, C.A.-L., 2021. Structural inheritance controls strain distribution during early continental rifting, Rukwa Rift. Front. Earth Sci. 9, 707869 https://doi.org/10.3389/feart.2021.707869.

Lavayssière, A., Drooff, C., Ebinger, C., Gallacher, R., Illsley-Kemp, F., Oliva, S.J., Keir, D., 2019. Depth extent and kinematics of faulting in the southern Tanganyika rift, Africa. Tectonics 38, 842–862. https://doi.org/10.1029/2018TC00537.

Lemna, O.S., Stephenson, R., Cornwell, D. ., 2019. The role of pre-existing Precambrian structures in the development of Rukwa Rift Basin, southwest Tanzania. J. Afr. Earth Sci. 150, 607–625. https://doi.org/10.1016/j.jafrearsci.2018.09.015.

Lezzar, K.E., Tiercelin, J.J., Turdu, C.L., Cohen, A.S., Reynolds, D.J., Gall, B.L., et al., 2002. Control of normal fault interaction of major Neogene sedimentary depocenters, Lake Tanganyika, East African rift. AAPG (Am. Assoc. Pet. Geol.) Bull. 86 (6), 1027–1059.

Macgregor, D., 2018. History of the development of Permian to Cretaceous rifts in East Africa: a series of interpreted maps through time. Petrol. Geosci. 24 (1), 8. https://doi.org/10.1144/petgeo2016-155, 2018.

Maestrelli, D., Montanari, D., Corti, G., Del Ventisette, C., Moratti, G., Bonini, M., 2020. Exploring the interactions between rift propagation and inherited crustal fabrics through experimental modeling. Tectonics 39, e2020TC006211. https://doi.org/10.1029/2020TC006211.

Michele, M., Di Stefano, R., Chiaraluce, L., Cattaneo, M., De Gori, P., Monachesi, G., Latorre, D., Marzorati, S., Valoroso, L., Ladina, C., Chiarabba, C., Lauciani, V., Fares, M., 2016. The Amatrice 2016 seismic sequence: a preliminary look to the mainshock and aftershocks distribution. Ann. Geophys. 59. Fast Track 5: The Amatrice seismic sequence: preliminary data and results.

Michon, L., Sokoutis, D., 2005. Interaction between structural inheritance and extension direction during graben and depocentre formation: an experimental approach. Tectonophysics 409 (1–4), 125–146. https://doi.org/10.1016/j.tecto.2005.08.020.

Michon, L., Famin, V., Quidelleur, X., 2022. Evolution of the East African Rift System from trap-scale to plate-scale rifting. Earth Sci. Rev. 231 https://doi.org/10.1016/j.earscirev.2022.104089.

Miller, J.F., Mitra, S., 2011. Deformation and secondary faulting associated with basement-involved compressional and extensional structures. Am. Assoc. Petrol. Geol. Bull. 95, 675–689.

Molnar, N.E., Cruden, A.R., Betts, P.T., 2019. Interactions between propagating rifts and linear weaknesses in the lower crust. Geosphere 15 (5), 1617–1640. https://doi.org/10.1130/GES02119.1, 2019.

Molnar, N.E., Cruden, A.R., Betts, P.T., 2020. The role of inherited crustal and lithospheric architecture during the evolution of the Red Sea: insights from three dimensional analogue experiments. Earth Planet Sci. Lett. 544, 116377 https://doi.org/10.1016/j.epsl.2020.116377.

Morley, C.K., 1999. Influence of Preexisting Fabrics on Rift Structure. Geosciences of Rift Systems-Evolution of East Africa, vol. 44. The American Association of Petroleum Geologists Studies in Geology, pp. 151–160. https://doi.org/10.1306/St44623.

Morley, C.K., Haranya, C., Phoosongsee, W., Pongwapee, S., Kornsawan, A., Wonganan, N., 2004. Activation of rift oblique and rift parallel pre-existing fabrics during extension and their effect on deformation style: examples from the rifts of Thailand. J. Struct. Geol. 26 (10), 1803–1829. https://doi.org/10.1016/j.jsg.2004.02.014.

Morris, A.P., Ferrill, D.A., Henderson, D.B., 1996. Slip tendency and fault reactivation. Geology 24, 275–278.

Neves, M.C., Paiva, L.T., Luis, J., 2009. Software for slip-tendency analysis in 3D: a plug-in for Coulomb. Comput. Geosci. 35, 2345–2352.

Nixon, C.W., Sanderson, D.J., Dee, S.J., Bull, J.M., Humphreys, R.J., Swanson, M.H., 2014. Fault interactions and reactivation within a normal-fault network at Milne Point, Alaska. AAPG (Am. Assoc. Pet. Geol.) Bull. 98 (10), 2081–2107.

Odinsen, T., Reemst, P., Beek, P.V.D., Faleide, J.I., Gabrielsen, R.H., 2000. Permo-Triassic and Jurassic extension in the northern North Sea:Results from tectonostratigraphic forward modelling. Geological Society, London, Special Publications 167, 83–103.

Osagiede, E.E., Rosenau, M., Rotevatn, A., Gawthorpe, R., Jackson, C.A.L., Rudolf, M., 2021. Influence of zones of pre-existing crustal weakness on strain localization and partitioning during rifting: insights from analog modeling using high-resolution 3D digital image correlation. Tectonics 40 (10). https://doi.org/10.1029/2021TC006970 e2021TC006970.

Phillips, T.B., Jackson, A.L., Bell, R.E., Duffy, O.B., Fossen, H., 2016. Reactivation of intrabasement structures during rifting: a case study from offshore southern Norway. J. Struct. Geol. 91, 54–73.

Pongwapee, S., Morley, C.K., Won-in, K., 2019. Impact of pre-existing fabrics and multi-phase oblique extension on cenozoic fault patterns, wichianburi sub-basin of the phetchabun rift, Thailand. J. Struct. Geol. 118, 340–361. https://doi.org/10.1016/j.jsg.2018.11.012.

Ramberg, H., 1981. Gravity, Deformation and the Earth's Crust. Academic Press, London.

Reber, J.E., Cooke, M.L., Dooley, T.P., 2020. What model material to use? A review on rock analogs for structural geology and tectonics. Earth Science Review 202. https://doi.org/10.1016/j.earscirev.2020.103107.

Riedel, W., 1929. Zur Mechanik Geologischer Brucherscheinungen, 1929 B. Centralbl. f. Mineral. Geol. u. Pal., pp. 354–368

Roberts, E.M., O'Connor, P.M., Stevens, N.J., Gottfried, M.D., Jinnah, Z.A., Ngasala, S., Choh, A.M., Armstrong, R.A., 2010. Sedimentology and depositional environments of the red sandstone group, Rukwa Rift basin, southwestern Tanzania: new insight into cretaceous and paleogene terrestrial ecosystems and tectonics in sub-equatorial Africa. J. Afr. Earth Sci. 57, 179–212. https://doi.org/10.1016/j.jafrearsci.2009.09.002.

Sibson, R.H., 1985. A note on fault reactivation. J. Struct. Geol. 7 (6), 751–754.

Spyropoulos, C., Griffith, W., Scholz, C., Shaw, B., 1999. Experimental evidence for different strain regimes of crack populations in a clay model. Geophys. Res. Lett. 26, 1081–1084.

Tchalenko, J.S., 1970. Similarities between shear zones of different magnitudes. Bull. Geol. Soc. Am. 81, 1625–1640.

Thielicke, W., Stamhuis, E.J., 2014. PIVlab e towards user-friendly, affordable and accurate digital particle image velocimetry in MATLAB. J. Open Res. Software 2 (1), e30. https://doi.org/10.5334/jors.bl.

Thielicke, W., 2014. The Flapping Flight of Birds e Analysis and Application. Phd thesis. Rijksuniversiteit, Groningen.

Tommasi, A., Vauchez, A., 2001. Continental rifting parallel to ancient collisional belts: an effect of the mechanical anisotropy of the lithospheric mantle. Earth Planet Sci. Lett. 185, 199–210. https://doi.org/10.1016/s0012-821x(00)00350-2.

Wang, L., Maestrelli, D., Corti, G., Zou, Y., Shen, C., 2021. Normal fault reactivation during multiple extension:analogue models and application to the turkana depression, east Africa. Tectonophysics 811, 228870. https://doi.org/10.1016/j.tecto.2021.228870.

Wedmore, L.N.J., Williams, J.N., Biggs, J., Fagereng, A., Mphepo, F., Dulanya, Z., et al., 2020. Structural inheritance and border fault reactivation during active early-stage rifting along the thyolo fault, Malawi. J. Struct. Geol. 139, 104097 https://doi.org/10.1016/j.jsg.2020.104097.

Whipp, P.S., Jackson, C.A.-L., Gawthorpe, R.L., Dreyer, T., Quinn, D., 2014. Normal fault array evolution above a reactivated ruft fabric; a subsurface example from the northern Horda Platform, Norwegian North Sea. Basin Res. 26, 523–549.

Willemse, E.J.M., 1997. Segmented normal fault: correspondence between three-dimensional mechanical models and field data. J. Geophys. Res. 102, 675–692.

Withjack, M.O., Olson, J., Peterson, E., 1990. Experimental models of extensional forced folds. AAPG (Am. Assoc. Pet. Geol.) Bull. 74 (7), 1038–1054.

Withjack, M.O., Henza, A.A., Schlische, R.W., 2017. Three-dimensional fault geometries and interactions within experimental models of multiphase extension. AAPG (Am. Assoc. Pet. Geol.) Bull. 101, 1767–1789. https://doi.org/10.1306/02071716090.

Withjack, M.O., Schlische, R.W., 2006. Geometric and experimental models of extensional fault-bend folds. Geochem. Soc. Spec. Publ. 253, 285–305.

Zwaan, F., Chenin, P., Erratt, D., Manatschal, G., Scheurs, G., 2021. Competition between 3D structural inheritance and kinematics during rifting: insights from analogue models. Basin Res. 1–31. https://doi.org/10.1111/bre.12642, 00.

Zwaan, F., Chenin, P., Erratt, D., Manatschal, G., Schreurs, G., 2022. Complex Rift patterns, a result of interacting crustal and mantle weaknesses, or multiphase rifting? Insights from analogue models. Solid Earth Discuss 12 (7), 1473–1495. https://doi.org/10.5194/se-12-1473-2021.

Zwaan, F., Schreurs, G., 2017. How oblique extension and structural inheritance influence rift segment interaction: insights from 4D analog models. Interpretation 5 (1), SD119–SD138. https://doi.org/10.1190/INT-2016-0063.1.

Zwaan, F., Schreurs, G., Buiter, S.J.H., 2019. A systematic comparison of experimental set-ups for modelling extensional tectonics. Solid Earth 10, 1063–1097. https://doi.org/10.5194/se-10-1063-2019.